Tomi Pulli

Improved Diffusers for Solar UV Spectroradiometers

School of Electrical Engineering

Thesis submitted for examination for the degree of Master of Science in Technology.

Espoo 26.10.2012

Thesis supervisor:

Prof. Erkki Ikonen

Thesis advisor:

D.Sc. (Tech.) Petri Kärhä

Aalto-yliopisto
Sähkötekniikan
korkeakoulu

AALTO UNIVERSITY
SCHOOL OF ELECTRICAL ENGINEERING

ABSTRACT OF THE
MASTER'S THESIS

Author: Tomi Pulli

Title: Improved Diffusers for Solar UV Spectroradiometers

Date: 26.10.2012 Language: English Number of pages: 9+48

Department of Signal Processing and Acoustics

Professorship: Measurement Science and Technology Code: S-108

Supervisor: Prof. Erkki Ikonen

Advisor: D.Sc. (Tech.) Petri Kärhä

Solar UV (ultraviolet) radiation scatters heavily in the atmosphere, and the diffuse component of the radiations accounts for a significant portion of the total UV radiation that reaches the surface of the Earth. Diffuser heads whose angular response is proportional to the cosine of the zenith angle are needed for the global irradiance measurements. In this thesis, a combination of measurements and simulations was used to optimize such a diffuser. At the first stage, test samples of various materials were measured for their diffuse transmittance properties in a goniometric setup to find out the most promising material candidate for use in an improved solar UV diffuser head. Quartz materials with gas bubbles that acted as scattering centers were found to be attractive alternatives to the traditional PTFE (polytetrafluoroethylene, Teflon) materials for this purpose. At the next stage, a Monte Carlo ray tracing software was developed to simulate light transport inside the diffusers. The software was validated by comparing measured and simulated results of the test samples. The effects of various simulation parameters on the overall angular response were studied extensively. The angular response was found to be highly sensitive to variations in some of the parameter values, highlighting the importance of low manufacturing tolerances during production. It was shown that an ideal cosine response cannot be attained without shaping the diffuser in one way or another, due to the refractive index difference between the diffuser material and its surroundings. An integrated cosine error of 1.6 % was reached with an optimized raised flat diffuser. An optimized diffuser with spherical front surface yielded the integrated cosine error of 0.63 %. This value is well below the integrated cosine errors of most UV diffusers currently in use.

Keywords: Radiometry, Solar UV, Diffusers, Monte Carlo analysis

AALTO-YLIOPISTO
SÄHKÖTEKNIIKAN KORKEAKOULU

DIPLOMITYÖN
TIIVISTELMÄ

Tekijä: Tomi Pulli

Työn nimi: Auringon UV-säteilyä mittaavan spektroradiometrin diffuuserin parantaminen

Päivämäärä: 26.10.2012 Kieli: Englanti Sivumäärä: 9+48

Signaalinkäsittelyn ja akustiikan laitos

Professuuri: Mittaustekniikka Koodi: S-108

Valvoja: Prof. Erkki Ikonen

Ohjaaja: TkT Petri Kärhä

Auringon ultravioletti- eli UV-säteily siroaa voimakkaasti ilmakehässä, minkä seurauksena UV-säteilyn epäsuora komponentti muodostaa merkittävän osan maan pinnalle saapuvasta kokonaissäteilystä. Diffuuseripäitä, joiden kulmavaste on verrannollinen zeniittikulman kosiniin, tarvitaan globaaleissa säteilyvoimakkuusmittauksissa. Työssä tämänkaltainen diffuuseri optimoitiin mittausten ja simulointien avulla. Ensimmäisessä vaiheessa lukuisten eri materiaaleista valmistettujen testinäytteiden diffuusiläpäisyominaisuudet mitattiin goniometrilaitteistossa, tavoitteena löytää lupaavin pohjamateriaali paranneltua diffuuseripäätä varten. Kvartsinäytteiden, joissa kaasukuplat toimivat sirontaytiminä, todettiin olevan houkuttelevia vaihtoehtoja perinteisille PTFE-materiaaleille (polytetrafluorieteeni, Teflon) tähän tarkoitukseen. Tutkimuksen seuraavassa vaiheessa kehitettiin Monte Carlo -ohjelma, jonka avulla simuloitiin valon etenemistä diffuuserin sisällä. Ohjelman toimivuus testattiin vertailemalla testinäytteiden mittaus- ja simulointituloksia keskenään. Eri simulointiparametrien vaikutusta kulmavasteeseen tutkittiin kattavasti. Kulmavasteen todettiin olevan erittäin herkkä tiettyjen parametriarvojen vaihteluille, mikä korostaa pienten toleranssien tärkeyttä diffuusereiden valmistusvaiheessa. Työssä osoitettiin, että täydellistä kosinivastetta ei voi saavuttaa muotoilematta diffuuseria tavalla tai toisella. Tämä on seurausta diffuuserimateriaalin ja sen ympäristön taitekerroinerosta. Optimoidulla nostetulla tasodiffuuserilla saavutettiin 1.6 %:n integroitu kosinivirhe. Vastaavasti optimoitu diffuuseri, jonka etupinta oli muotoiltu pallomaisesti, tuotti 0.63 %:n integroidun kosinivirheen. Arvo on selvästi matalampi kuin suurimmalla osalla tällä hetkellä käytössä olevista UV-diffuusereista.

Avainsanat: Radiometria, Auringon UV, Diffuuserit, Monte Carlo -analyysi

Preface

The work leading to this thesis was carried out in Metrology Research Institute (MRI) of Aalto University School of Electrical Engineering. The work was partly funded by The European Metrology Research Programme (EMRP) ENV03 Project ”Traceability for surface spectral solar ultraviolet radiation”. I would like to thank all the parties involved for the opportunity to be a part of this project.

I am grateful to Professor Erkki Ikonen for supervising this thesis as well as for the possibility to work on this and many other interesting subjects. Special thanks goes to my instructor, Dr. Petri Kärhä, for his constant support and constructive feedback throughout this thesis. I also appreciate the help I got from Dr. Farshid Manoocheri and Priit Jaanson during the laborious fluorescence measurements. In fact, I would like to thank the entire staff of the Metrology Research Institute for the relaxed, supportive, and constructive working environment in which one never had to be alone with his problems.

The material samples necessary to carry out this work were provided by Dr. Josef Schreder of CMS – Ing. Dr. Schreder GmbH and by Joop Mes of Kipp & Zonen. I want to thank them for this support as well as for the many insightful discussions regarding diffuser design.

Last but not least, I’m deeply grateful to my family for the invaluable support they have given me throughout my studies, and in fact my whole life.

Otaniemi, 26.10.2012

Tomi P. Pulli

Contents

Symbols and abbreviations **vii**

1 Introduction **1**

2 Diffuser structure **3**
2.1 Detector designs 3
2.2 Diffuser materials 6
2.3 Quality of diffusers 6

3 Material characterization **8**
3.1 Diffuser samples 8
3.2 Goniometric measurements 8
3.2.1 Measurement setup 8
3.2.2 Measurement procedure and results 11
3.3 Fluorescence measurements 13
3.3.1 Measurement setup 13
3.3.2 Measurement procedure and results 15

4 Diffuser simulation software **18**
4.1 Monte Carlo method 18
4.2 Technical details of the software 19
4.3 Detector structure 20
4.4 Simulation flow 22
4.5 Propagation and absorption 23
4.6 Scattering 25
4.7 Reflection and refraction 26
4.8 Weather dome 29

5 Simulation results **31**
5.1 Measured and simulated angular responses 31
5.2 Effects of various parameters on the angular response 32
5.2.1 Refractive index 32
5.2.2 Diffuser dimensions 33
5.2.3 Diffuser curvature 35
5.2.4 Shadow ring 36
5.2.5 Clear area of the diffuser 37

5.2.6 Weather dome . . . 39

5.3 Diffuser optimization . . . 39

5.3.1 Optimization process . . . 39

5.3.2 Optimized diffuser designs . . . 42

6 Conclusions **44**

References **46**

Symbols and abbreviations

Symbols

d	diameter of the diffuser
d_{beam}	diameter of the clear area of the diffuser
d_{sr}	diameter of the shadow ring
f_2	integrated cosine error
$f_2(\theta)$	cosine error as a function of the zenith angle θ
g	scattering anisotrophy parameter
h	height of the diffuser
h_{sr}	height of the shadow ring
h_{sw}	height of the sidewall
m	termination roulette parameter
N	number of samples in simulation
n_1, n_2	refractive indices of the the first and the second materials
n_{dom}	refractive index of the weather dome
$\tilde{\mathbf{n}}$	normal vector of the surface
$\tilde{\mathbf{n}}_{\mathbf{sph}}$	normal vector of the spherical surface
$\tilde{\mathbf{n}}_{\mathbf{sw}}$	normal vector of the sidewall surface
$\tilde{\mathbf{n}}_{\mathbf{f,i}}$	normal vector of the flat front or back surface
R	reflectance
R_{in}	reflectance at the inner surface of the dome (approximation)
$R_{\text{in},i}$	reflectance at the inner surface of the dome in the ith stage
R_{out}	reflectance at the outer surface of the dome (approximation)
$R_{\text{out},i}$	reflectance at the outer surface of the dome in the ith stage
R_{tot}	total reflectance of the weather dome
r	radius of the diffuser
r_{dom}	radius of the weather dome
r_{sph}	radius of curvature of the spherical surface of the diffuser
$S(\theta)$	signal level of the detector at incident angle θ
s	step size, propagation distance
s_{sph}	distance to the spherical surface of the diffuser
s_{sw}	distance to the sidewall of the diffuser
$s_{\text{f},i}$	distance to the flat front or back surface of the diffuser
s_{min}	distance to the nearest surface of the diffuser
$\tilde{\mathbf{s}}_{\mathbf{incident}}$	unit vector in the direction of incident particle

$\tilde{\mathbf{s}}_{\mathbf{reflect}}$	unit vector in the direction of reflected particle
$\tilde{\mathbf{s}}_{\mathbf{refract}}$	unit vector in the direction of refracted particle
T	transmittance
T_{in}	transmittance at the inner surface of the dome (approximation)
$T_{\mathrm{in},i}$	transmittance at the inner surface of the dome in the ith stage
T_{out}	transmittance at the outer surface of the dome (approximation)
$T_{\mathrm{out},i}$	transmittance at the outer surface of the dome in the ith stage
T_{tot}	total transmittance of the weather dome
t	thickness of the diffuser
t_{dom}	thickness of the weather dome
W	weight of the particle
ΔW	change in the weight of the particle
W_{th}	termination threshold weight
x	x coordinate of the particle
x_{s}	x coordinate at the material interface
y	y coordinate of the particle
y_{s}	y coordinate at the material interface
z	z coordinate of the particle
$z_{\mathrm{f},i}$	z coordinates of the front or back surfaces of the diffuser
z_{s}	z coordinate at the material interface
z_{det}	distance between the detector and the diffuser
z_{dom}	offset of the weather dome
z_{sph}	offset of the spherical surface of the diffuser
α	deflection angle of the particle
β	azimuthal scattering angle of the particle
θ	incident, zenith angle
θ_{sr}	zenith angle above which the shadow ring affects the response
μ_{a}	absorption coefficient
μ_{s}	scattering coefficient
μ_{x}	x component of the directional cosine of the particle
μ_{y}	y component of the directional cosine of the particle
μ_{z}	z component of the directional cosine of the particle
ν_1	incident angle of the particle
ν_2	refraction angle of the particle
$\phi(\alpha)$	scattering phase function
χ	uniformly distributed random number in the interval [0,1)

Abbreviations

CIE	Commission internationale de l'éclairage (International Commission on Illumination)
EMRP	The European Metrology Research Programme
HeCd	Helium Cadmium
MIKES	Mittatekniikan keskus (Centre of Metrology and Accreditation)
MRI	Metrology Research Institute
ND	Neutral density
PTFE	Polytetrafluoroethylene, brand name Teflon by DuPont Co.
PMT	Photomultiplier tube
RNG	Pseudo-random number generator
SFMT	SIMD-oriented Fast Mersenne Twister
SIMD	Single instruction, multiple data
UV	Ultraviolet

1 Introduction

Ultraviolet (UV) radiation has both beneficial and harmful effects on human health. The former are largely related to vitamin D production in the skin induced by UV exposure. The most significant health concerns of UV exposure are erythema (reddening of the skin, sunburn) and different forms of skin cancer. Accurate solar UV measurements are therefore important for both research and public health purposes. [1]

The devices for measuring solar UV radiation can be divided into two main categories: spectral instruments [2] and broadband instruments [3]. As vitamin D production, erythema and melanoma each have their characteristic action spectra [4, 5], special filters are required in broadband measurements. Typically erythema weighting is utilized. In case of wavelength resolved measurements, this weighting can be performed during the data analysis. The structure of a typical broadband instrument is relatively simple as compared to that of a typical spectral instrument, and the detector unit can often be placed directly behind the entrance optics of the device. In spectral instruments the radiation is typically guided to the detector via an optical fiber or a fiber bundle – such as with Bentham spectroradiometer – or through a set of mirrors – such as with Brewer spectroradiometer.

Solar UV radiation scatters heavily in the atmosphere: in one study the diffuse component was found to account for 23 % to 59 % of the total solar UV radiation in the range 280–320 nm (UVB) and 17 % to 31 % in the range 320–400 nm (UVA) [6]. Therefore, in order to determine the amount of UV radiation that reaches the surface of the Earth, global irradiance, which is a combination of the direct and the diffuse radiation, needs to be measured. High quality entrance optics are needed for these measurements in case of both spectral and broadband instruments.

The angular response of an ideal detector is proportional to the cosine of the zenith angle, i.e. the angle between the incoming radiation and the surface normal of the detector. Furthermore, the angular response should be independent of the azimuth angle of the incoming radiation. A deviation from the cosine response can cause significant errors in global irradiance measurements. By estimating the angular distribution of the radiation at the time of the measurement, a correction to the measurement result can be calculated. In one study, cosine corrections on the order of 9–20 % were found necessary for one spectroradiometer measuring global spectral irradiance [7]. Unfortunately, this approach has a limited accuracy only [7, 8]. Therefore, the quality of the entrance optics remains of utmost importance for accurate global irradiance measurements.

The goal of this thesis was threefold: First, the suitability of new quartz based materials [9] as diffusers was to be studied by characterizing various material samples for their scattering, transmission and fluorescence properties. The second goal was to develop a model and a software for simulating light transport inside the diffusers. Finally, the software was to be used to optimize the structure of a detector head to be used in a solar UV spectroradiometer. While this thesis focuses on solar UV radiometers, the results of the simulations are equally valid for photometer heads utilizing a diffuser.

In Section 2, the basic structure of a diffuser head for spectral irradiance measurements is described. A short overview of the properties of common diffuser materials is given. The method for characterizing the performance of the diffusers and the current state of the art of the detector heads are also briefly discussed in this section.

Section 3 is dedicated to measurements. Six PTFE samples (polytetrafluoroethylene, brand name Teflon) and seven synthetic quartz samples were characterized for their light diffusing and transmission properties in a goniometric setup utilizing a HeCd laser at 325 nm and 442 nm wavelengths. The fluorescence of selected materials was studied in a commercial fluorescence spectrometer. The results were used to find out the best material for use in the improved diffuser as well as to determine the relevant material parameters for modeling the diffusers. The two measurement setups are presented and the measurement results discussed.

The structure and the operating principles of the Monte Carlo diffuser simulation software are discussed in Section 4. The measured and the simulated results are compared in Section 5 in order to validate the software. The effects of different detector parameters on the overall angular response of the detectors were studied extensively. The results of these simulations are also detailed in this section. Finally, two optimized diffuser designs – one raised flat diffuser and one spherically shaped diffuser – for a detector head with a fiber entrance are presented.

2 Diffuser structure

In this section, a brief overview of solar UV diffusers is given. First, typical diffuser geometries and detector components are detailed. The advantages and drawbacks of common diffuser materials are also considered. Finally, the performance characterization of the detector heads is discussed.

2.1 Detector designs

One way to achieve a good angular response is to use an integrating sphere (see Figure 1) in the entrance of the detector. Integrating sphere detectors are typically quite complicated and expensive. Therefore, at least in solar UV measurements, a more common approach is to place a sheet of diffusing material in front of the detector. Typical material choices include PTFE, roughened quartz and opal glass.

Figure 1: Integrating sphere with two entrance ports open. Global irradiance can be measured by exposing one of the ports to radiation and measuring the light level inside the sphere through the second port. Purpose-built integrating sphere detector heads for spectral irradiance measurements are commercially available.

Figure 2 shows schematically the basic structures of diffusers used with spectroradiometers. The angular response of a detector with a simple flat disk of diffusing material shown in Figure 2(a) deviates considerably from the cosine function: the response is too small at large zenith angles. The simplest, and also the cheapest, modification to improve the cosine response is to raise the diffuser disk relative to the housing of the detector, as illustrated schematically in Figure 2(b). A photograph of such a detector head is shown in Figure 3(a). This modification increases the angular response especially at large incident angles, because the sidewalls of the diffuser are now partially exposed to the radiation. To avoid light from reaching the detector at incident angles equal to and larger than 90°, a so-called ”shadow ring” is typically placed around the diffuser – see Figure 2(b). The shadow ring also affects the shape of the angular response at large incident angles.

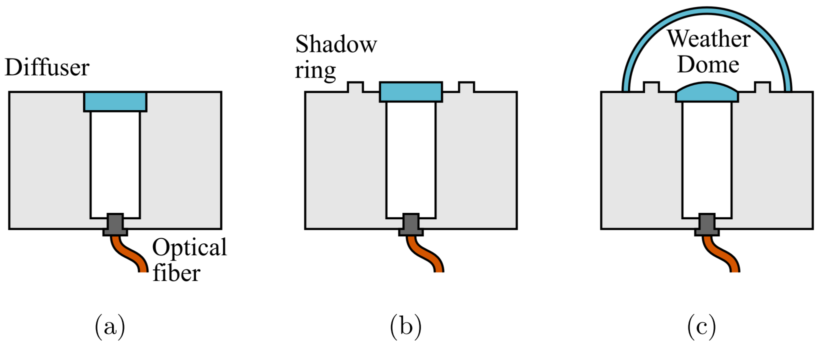

Figure 2: Illustrations of typical diffuser head structures: (a) a flat diffuser, (b) a raised diffuser, and (c) a shaped diffuser. Quartz weather dome can be incorporated in all designs. Depending on the type of the device, the optical fiber may be replaced by a photodetector or a set of mirrors that guides the light to the detector unit.

Further improvements in angular response can be achieved by shaping the diffuser, as shown schematically in Figure 2(c). An example of a more complicated diffuser shape is shown in Figure 3(b). When designing more exotic diffusers, the price and manufacturability of the structure needs to be taken into consideration.

Diffuser materials are sensitive to weather and contamination. Therefore, a protective weather dome is placed in front of the diffuser in outdoor measurements, as seen in Figure 2(c). These quartz structures are quite expensive and as a consequence, they are typically not incorporated in detector heads that are used solely indoors. Figure 4 shows a detector with a weather dome.

In most detector systems, the transmitted light is guided to the detection unit via an optical fiber, a fiber bundle, or through a series of mirrors and/or lenses. The acceptance angle of the fiber (or equivalent) and the clear area of the diffuser are important parameters to consider when optimizing the diffusers.

(a) (b)

Figure 3: Photograph of (a) PRC Krochmann photometer head with raised diffuser and (b) Konica Minolta T-10A illuminance meter with shaped diffuser [Konica Minolta website].

Figure 4: Kipp & Zonen UV radiometer with a protective weather dome [Kipp & Zonen website].

2.2 Diffuser materials

PTFE is the most common material used in solar UV diffusers. It has good light diffusing properties, but also some drawbacks. For example, the transmittance of PTFE is relatively low, which can cause problems in signal detection. PTFE also undergoes a change in the crystal structure at a temperature of about 19 °C. The phase transition causes the transmittance of the material to drop abruptly by 1 % to 3 % below the transition temperature [13]. This phenomenon needs to be taken into account when calibrating the device, as the indoor calibration conditions can differ significantly from the outdoor measurement conditions. The transition also considerably increases the uncertainty of solar UV measurements at outdoor temperatures close to 19 °C.

Lately, synthetic quartz based materials with tiny gas bubbles have been introduced. They are interesting candidates for new diffuser materials [9]. The gas bubbles act as scattering centers for photons. By varying the size and the density of the bubbles, the scattering and the light transmission properties of the material can be varied. The transmittance of these materials is higher than that of PTFE samples of similar thickness. The possibility to increase the thickness of the sample without sacrificing the signal-to-noise ratio makes it easier to optimize the diffuser shape, because the sidewalls of the sample will have larger effect on the angular response. Quartz does not exhibit similar abrupt temperature effects as PTFE in the temperature range relevant to the solar UV measurements. Finally, polished quartz diffusers are expected to be easier to clean than PTFE diffusers, which suggests that expensive weather domes might not be required with these materials. The major drawback of bubbled quartz materials is that they are relatively expensive to manufacture.

2.3 Quality of diffusers

The quality of the entrance optics is typically characterized by its cosine error

$$f_2(\theta) = \left[\frac{S(\theta)}{S(0^\circ)\cos(\theta)} - 1\right] \cdot 100\ \% \ , \tag{1}$$

where $S(\theta)$ is the measured signal at the zenith angle θ. This form assumes the angular response to be independent of the azimuth angle. The integrated cosine error, as defined in CIE technical report [10], can be calculated as

$$f_2 = \int_{0^\circ}^{85^\circ} |f_2(\theta)| \sin(2\theta) \, d\theta \; . \tag{2}$$

The weighting term $\sin(2\theta) = 2\cos(\theta)\sin(\theta)$ ensures that the contribution of the integrand goes to zero at large zenith angles, where the effective area of the diffuser approaches zero, as well as at small zenith angles, where the cone of angles of the spherical coordinate system approaches zero. Parameter f_2 gives the fractional error caused by the non-ideal angular response of the diffuser head under the assumption that the radiance is constant [10].

Large variation is to be found in the quality of the angular response of the detectors measuring global irradiance. In one study, the integrated cosine errors f_2 of four Brewer spectroradiometers with flat PTFE diffusers were found to range from 4 % to 15 % [11]. The quality of angular response was significantly improved by replacing the standard diffuser with a shaped PTFE diffuser, resulting in an integrated cosine error of 2.4 %.

According to the manufacturer, the typical integrated cosine error of a flat Bentham D6/D7 diffuser with an optical fiber entrance is around 0.75 % with the maximum integrated cosine error below 1 %. The typical and the maximum integrated cosine errors for the environmentally protected model of the same instrument are 1.5 % and 2.0 %, respectively. [12] This can be considered the current state of the art of UV diffuser heads.

3 Material characterization

The angular response of various diffuser samples was measured in a goniometric setup. In addition, fluorescence measurements were performed for selected samples. The purpose of these measurements was to find out the most promising material for use in the new improved diffuser design as well as to obtain the material parameters required for modeling the diffusers.

3.1 Diffuser samples

To find the most suitable material for use in the improved diffuser, two types of PTFE samples of varying thickness (five samples in total) and five types of synthetic bubbled quartz samples of varying thickness and diameters (seven samples in total) were characterized. For comparison, the light diffusing properties of the existing Brewer MK III PTFE diffuser head were studied as well. The samples are listed in Table 1 along with their thicknesses. A photograph of the samples is shown in Figure 5. Apart from Quartz E and the 1 mm thick Quartz B, all of the quartz samples were surface polished.

Table 1: List of diffuser samples

Name	**Thickness**	**Name**	**Thickness**
Quartz A	1.0 mm	PTFE A	0.5 mm
Quartz A	2.0 mm	PTFE A	1.0 mm
Quartz B	1.0 mm	PTFE A	2.0 mm
Quartz B	2.0 mm	PTFE B	0.5 mm
Quartz C	2.0 mm	PTFE B	1.0 mm
Quartz D	2.0 mm	Brewer	<0.5 mm
Quartz E	2.3 mm		

3.2 Goniometric measurements

3.2.1 Measurement setup

The measurement setup for the angular characterization of the diffuser materials is presented schematically in Figure 6. A photograph of the detector side of the setup is shown in Figure 7. A CVI Melles Griot Series 56 helium cadmium (HeCd) laser was used as the light source. The device produced two laser lines, one at the UV

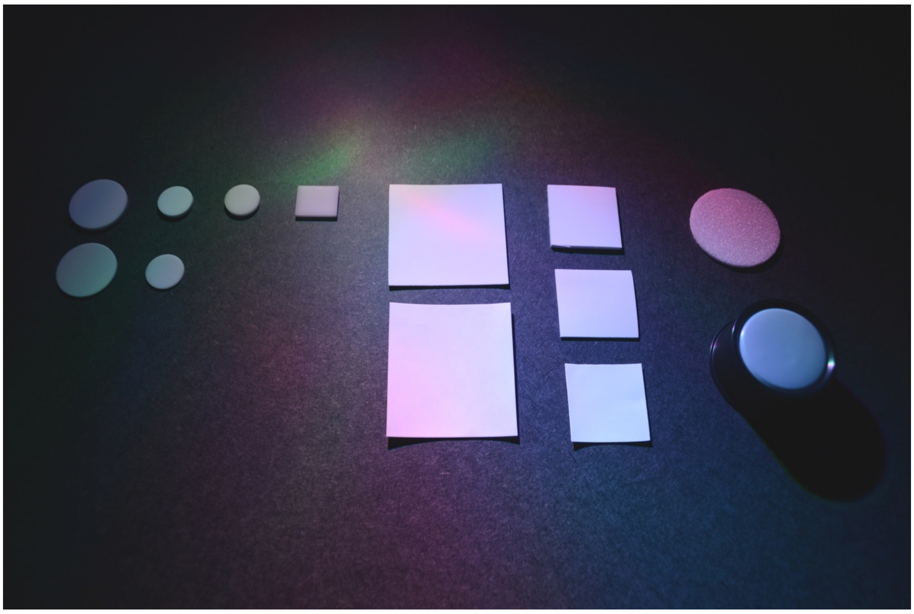

Figure 5: Photograph of the diffuser samples that were characterized. From left to right: 2x Quartz A, 2x Quartz B, Quartz C, Quartz D, 2x PTFE B, 3x PTFE A, Quartz E, and Brewer diffuser head.

region (wavelength 325 nm) and the other at the blue region (wavelength 442 nm). Filters in front of the output aperture of the laser were used to select one of the wavelengths at a time. A beam expander enlarged the beam to a diameter of 30 mm in order to overfill the sample. The beam expander consisted of two plano-convex lenses of focal lengths 50 mm and 350 mm located 400 mm apart from each other, resulting in a magnification of 7.

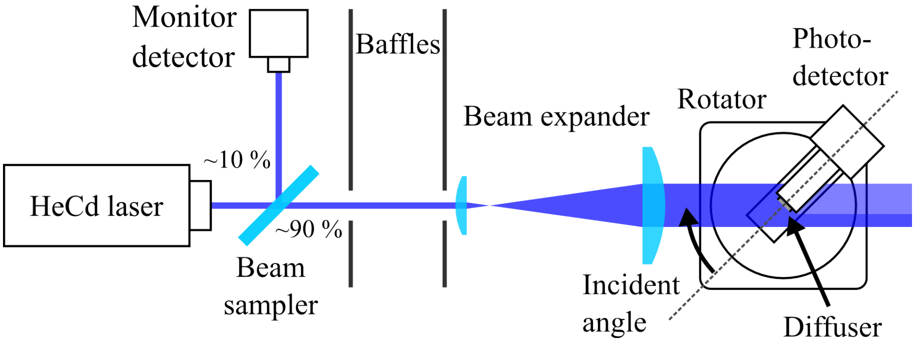

Figure 6: Structure of the goniometric measurement setup.

A monitor detector in combination with a beam sampler was used to track the long term stability and the short term fluctuations of the laser power. A set of baffles and adjustable irises between the beam sampler and the diffuser prevented

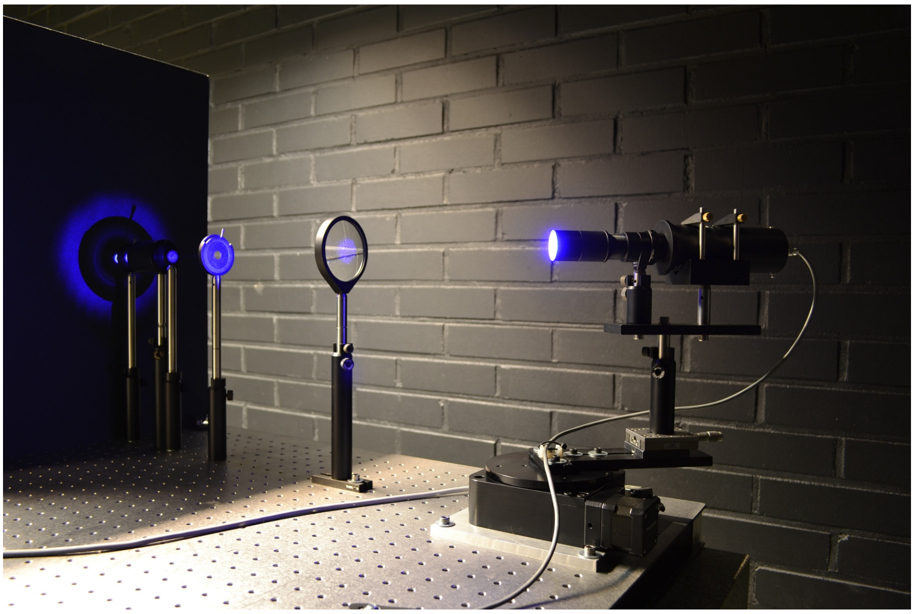

Figure 7: Photograph of the goniometric measurement setup.

the light scattered from the beam sampler and the monitor detector from reaching the diffuser. These baffles also blocked any stray light on the source side of the measurement setup. The distance between the source and the diffuser was about 2 meters.

Each material sample was, one at a time, installed into a prototype detector presented schematically in Figure 8. As the samples were of varying shapes and sizes (Figure 5), each had to be attached to the detector in a different way. Nevertheless, the 15 mm optics adapter was kept in place throughout all the measurements to keep the clear area of the diffuser constant, approximately 13 mm in diameter. Furthermore, the sides of the diffusers were always covered to prevent light transmission through the sidewalls of the diffuser. The Brewer diffuser was measured by sliding it on top of the lens tube with the 15 mm optics adapter still in place. The adjustable iris between the photodetector and the diffuser was fixed at an opening of 2.0 mm.

The photocurrent signal of the Hamamatsu S1226 photodiode used as the detector was converted into a voltage signal with a Lab Kinetics SP042 current-to-voltage converter. The output voltage was then measured with an Agilent 34410 digital multimeter. The photocurrent of the monitor detector was logged with an Agilent 34401 digital multimeter. The prototype detector was mounted on a Newmark RT-5 rotatory stage to control the incident angle. The angle between the photodetector and the diffuser normals was fixed at 0°. The rotary stage was connected to a Newmark NSC-M multiaxis motion controller. An automated measurement software

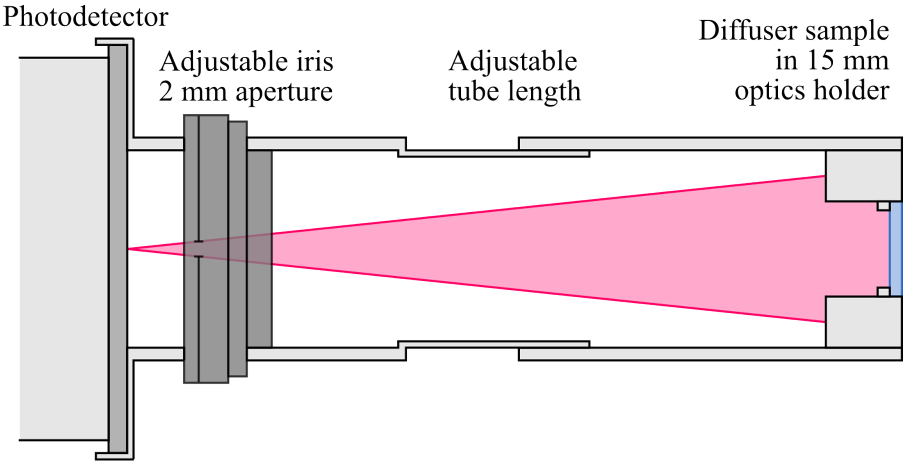

Figure 8: Structure of the prototype detector constructed of standard 1″ lens tubes.

was constructed using National Instruments' Labview.

3.2.2 Measurement procedure and results

Before the measurement, the diffuser sample was aligned so that its front surface coincided with the rotation axis of the turntable. The angular alignment of the prototype diffuser was verified from the reflection of the HeCd beam. The diffuser was positioned in the center of the expanded beam.

In the beginning of the measurement sequence, the offset signals of the detectors were measured by blocking the laser beam. After the dark signal measurement, one of the laser wavelengths was selected with the filter and the goniometric measurement was initiated. The angular response of the prototype detector was determined by rotating the detector at 1° intervals from $-90°$ to $90°$ with respect to the expanded laser beam. All samples were measured at both 325 nm and 442 nm wavelengths. The angular responses of Quartz C and Quartz D samples at the wavelength of 325 nm are presented in Figure 9 as examples. The differences between the angular responses at 325 nm and 442 nm wavelengths were found to be relatively small.

To compare the light diffusing properties of the material samples, the integrated cosine error of equation (2) was calculated for each sample. To rank the samples according the amount of transmitted light, the integrated photocurrent over the measured angular range was calculated for each sample. This value was then divided by the average monitor detector current to account for possible laser power fluctuations between the measurements. Finally, the average of the integrated signals over all samples was calculated and the values were normalized to this average.

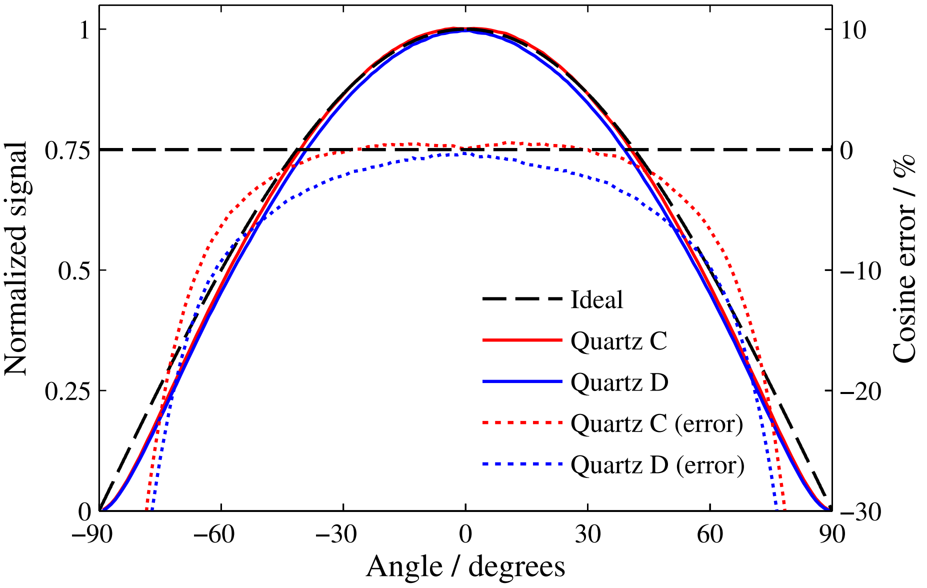

Figure 9: Measured angular responses and the cosine errors of Quartz C and Quartz D samples in a prototype detector at the wavelength of 325 nm. Also plotted is the ideal cosine response.

In Figure 10 the diffuser materials are ranked according to their integrated cosine error and the integrated signal level.

The thickness of the diffuser significantly affected the amount of light transmitted by the sample but generally had little effect on the shape of the angular response. An exception to this rule were the two Quartz B samples whose angular responses differed significantly from each other. This finding can most likely be attributed to the fact that the two samples were of different finish: the 2 mm sample was surface polished whereas the 1 mm sample was not. While the integrated cosine errors of the two PTFE B samples deviated considerably from each other, the shapes of their angular responses were almost identical.

The unpolished Quartz sample E was clearly unsuitable for use as a UV diffuser due to its poor angular response. Apart from this outlier, the quartz materials had, in general, smaller cosine error and higher transmission than the PTFE diffusers of equal thickness. Quartz C had the smallest cosine errors among all the studied materials as well as very impressive transmittance when taking into account the thickness of the sample. For these reasons, Quartz C was selected as the base material for the improved diffuser head. The cosine response of the current Brewer diffuser was the best among all the PTFE samples that were studied and it transmitted more light

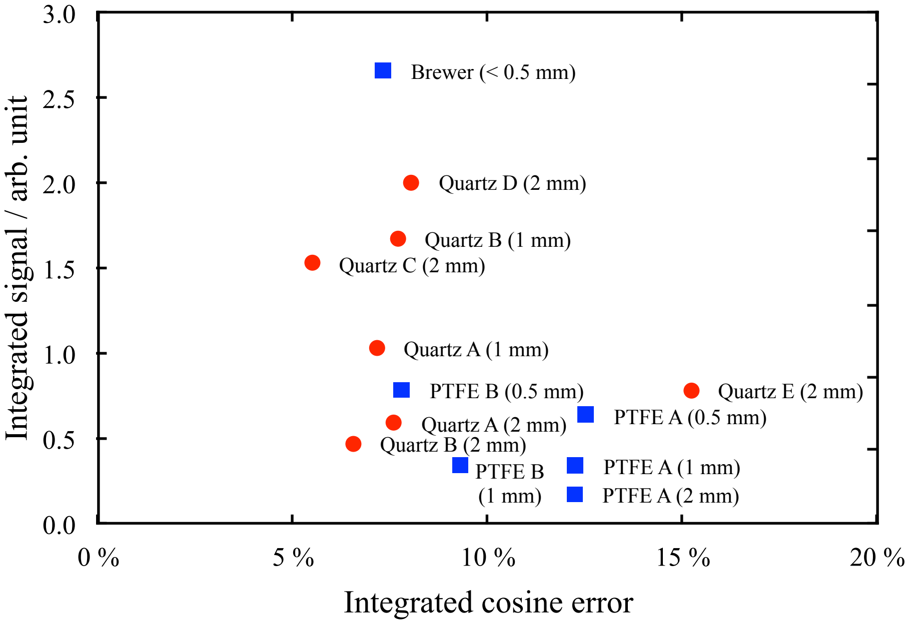

Figure 10: The integrated signal level versus the integrated cosine error for each quartz (red circles) and PTFE (blue squares) sample at 325 nm.

than any other sample. The sample was also the thinnest of the measured samples.

3.3 Fluorescence measurements

3.3.1 Measurement setup

For a material to be suitable as a UV diffuser, it has to be free of fluorescence. The fluorescence of the materials was measured with a commercial fluorescence spectrometer Perkin-Elmer LS-55. The working principle of the device is illustrated in Figure 11. A pulsed Xenon lamp acted as the light source and a photomultiplier tube (PMT) was used as the detector. Two monochromators, one at the source side and the other at the detector side, were used to select the excitation and the emission (detection) wavelengths, respectively. Two adjustable slits set the spectral width of the excitation and detection.

The diffuse reflected component of the excitation wavelength from the sample can significantly distort the measurement results. To avoid seeing large signal peaks at the excitation wavelength and its harmonics, a highpass filter can be placed in front of the beam before the emission grating. If the signal level is so high as to saturate the PMT, a 1 % neutral density (ND) filter can be used instead of one of

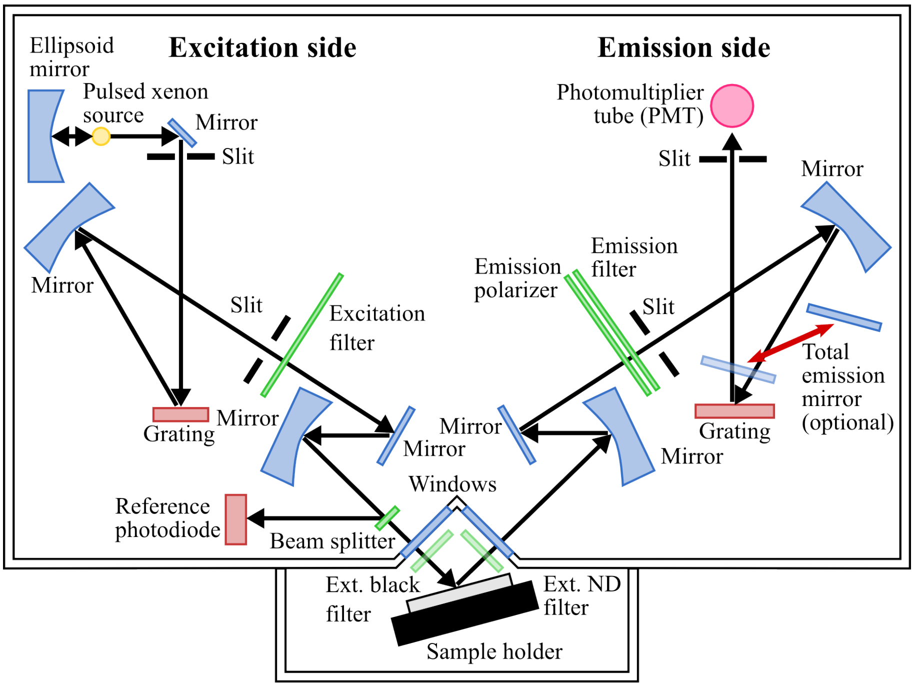

Figure 11: Structure of the Perkin-Elmer LS-55 fluorescence spectrometer. External black filter and external ND filter are also shown in the figure. (Redrawn and modified from the schematic in the device user manual.)

the highpass filters. The monochromators, the slits and the internal filters are all controlled in the measurement software.

Considerable amount of visible light reached the samples even when the excitation monochromator was set to UV wavelengths. This is evident from the solid lines of Figure 12 where the results of an emission scan at three different excitation wavelengths – 250 nm, 280 nm, and 300 nm – for the Brewer diffuser are presented. A 340 nm highpass filter was used on the emission side and both the excitation and the emission slits were set at 5 nm bandwidth.

To confirm that the signal was indeed caused by light leakage and not fluorescence, an external black lowpass filter (see Figure 11) was placed between the excitation monochromator and the sample. The results of the repeated measurements are shown in Figure 12 as dashed lines. The signal level above 420 nm dropped significantly, confirming that the signal was indeed caused by the diffuse reflection of the light that leaks from the excitation monochromator – not fluorescence. The signal peak at approximately 380 nm wavelength was caused by the white light component that passes through both the external black filter and the 340 nm emission filter. The second peak at 780 nm was caused by the harmonic of the first peak. These residual components were present in all the measurement and need to be taken into account when interpreting the results.

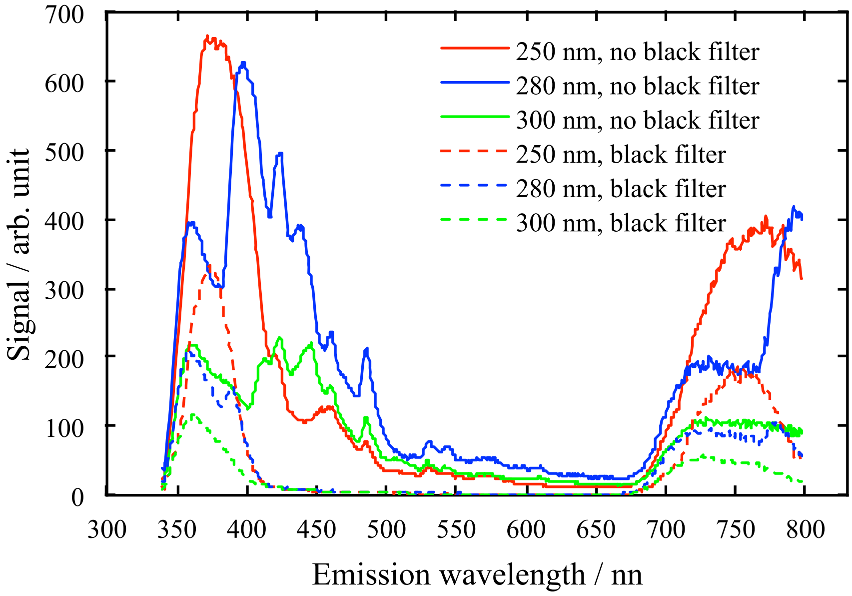

Figure 12: Emission scans at various excitation wavelengths for the Brewer diffuser. The effect that the black excitation filter has on the signal level highlights the light leakage problem of the excitation monochromator.

3.3.2 Measurement procedure and results

The fluorescence of the Quartz A and the PTFE B samples as well as that of the existing Brewer diffuser was measured. Quartz A was chosen for the fluorescence characterization instead of Quartz C, which was previously found to be best suited as a diffuser, because of the larger diameter of Quartz A sample. As the only difference between the Quartz samples A to D was the size and density of the gas bubbles, the fluorescence measurement results of Quartz A should be valid for all these samples.

The samples were aligned so that the specular reflection from the sample surface would not reach the detector. The signal level depended strongly on the sample position, namely the distance from the input and output windows. The optimal position was determined by moving the sample towards and away from the device on a linear translation stage until the signal maximum was found. This procedure was repeated for each diffuser separately.

The black filter was held in between the excitation monochromator and the sample in all the measurements to eliminate as much of the white light leakage as possible. The excitation slit was set to 5 nm, while the emission slit was set to 10 nm to maximize the detector signal. A 390 nm highpass filter was used in the emission side of the device.

The excitation scan was performed by replacing the emission grating with a total emission mirror, and scanning through the excitation wavelengths 250–360 nm. No definite fluorescence peaks were discovered for any of the diffusers. In fact, the shapes of the curves were identical for all of the samples, which suggests that the excitation scan is dominated by the leftover light leakage. The non-flat shape of the signal in the excitation scan can be attributed to the fact that the amount of white light leakage varies as a function of the wavelength, as is evident from Figure 12.

The emission scans from 340 nm to 800 nm were performed at three excitation wavelengths, namely 250 nm, 280 nm and 300 nm. The measurement results at 280 nm excitation are given as examples in Figure 13. The signals are normalized to the signal level at the reflection peak. To measure this excitation peak, the signal level had to be attenuated considerably. In addition to the internal 1 % ND filter, an external ND filter that dropped the signal level to about one fourth of the original was required. The emission slit was also changed from 10 nm to 2.5 nm, which was found to reduce the signal level approximately by a factor of 20. The measured signals around the 280 nm excitation (reflection) peak are presented for each diffuser in Figure 14.

In Figure 13, the normalized emission signal level of the PTFE B sample is significantly higher than that of the other two diffusers. However, the fact that the shape of the curve is identical to that of the other two samples suggests that the effect is not caused by fluorescence. The difference can, for example, be due to a problem in the normalization of the signals or the wavelength dependence of the reflectance.

Ignoring the signal peak caused by the leftover of the light leakage of the excitation monochromator, the detected signal levels were very low and no definite fluorescence peaks were visible. Based on the results, the possible fluorescence is at least 5 orders of magnitude below the intensity of the diffuse reflected component of the excitation wavelength.

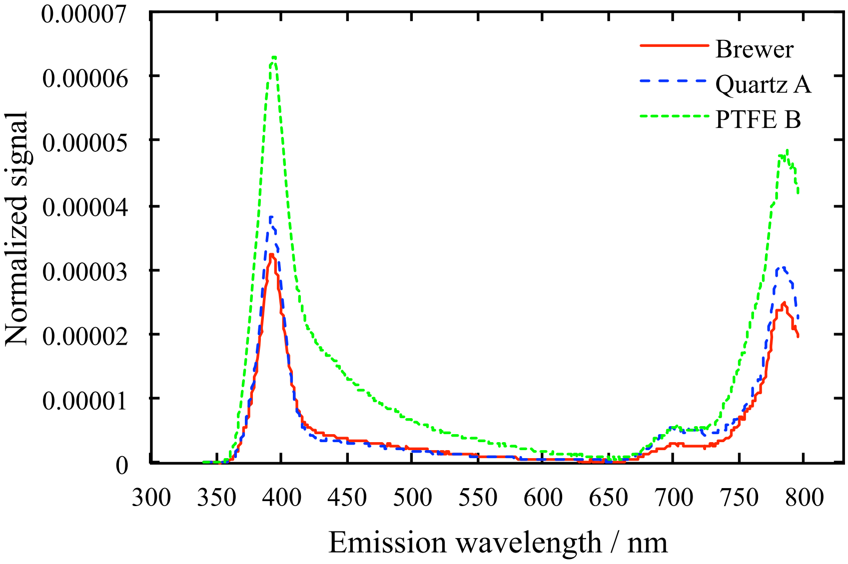

Figure 13: Normalized signal level as a function of the emission wavelength at 280 nm excitation for each diffuser. The results were normalized to the measured signal level of the diffuse reflection of the excitation peak.

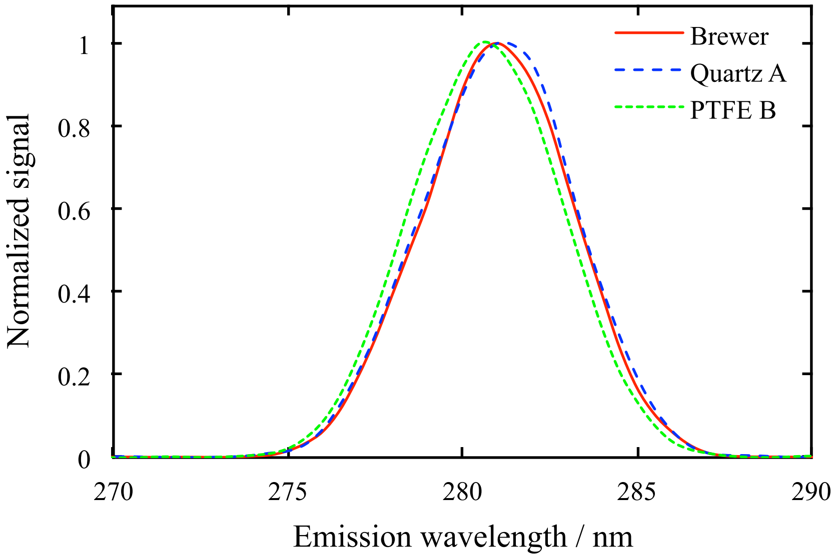

Figure 14: Normalized signal level around the reflected excitation peak.

4 Diffuser simulation software

In this section, the diffuser optimization software is detailed. The software is based on Monte Carlo ray tracing. Therefore, a brief historical introduction to the method is given. A more detailed description on the Monte Carlo method can be found in one of the many books dedicated to the subject [14, 15, 16]. Later, the structure and the operating principle of the software are discussed in detail.

4.1 Monte Carlo method

Monte Carlo method is a statistical sampling technique developed by Stanisław Ulam, John von Neumann, and Nicholas Metropolis [17] in mid-1940s at Los Alamos National Laboratory – the home of the atomic bomb. The method borrows its name from the famous casino in Monaco, frequently visited by Ulam's uncle [18]. The principle of the Monte Carlo method is nicely illustrated in Ulam's quote [19] on the origin of the idea:

> The first thoughts and attempts I made to practice [the Monte Carlo method] were suggested by a question which occurred to me in 1946 as I was convalescing from an illness and playing solitaires. The question was what are the chances that a Canfield solitaire laid out with 52 cards will come out successfully? After spending a lot of time trying to estimate them by pure combinatorial calculations, I wondered whether a more practical method than "abstract thinking" might not be to lay it out say one hundred times and simply observe and count the number of successful plays.
>
> — **Stanisław Ulam, 1983**

In the example, a rather involved problem of probabilities is transformed into a simple game of repetition. Provided that the algorithm knows the rules of the game and that the cards drawn from the deck follow the correct distribution, then after multiple games of solitaire, the chances of successful ending can be estimated with some accuracy.

What can be extracted from the thought experiment on solitaire, holds true for Monte Carlo algorithms in general. Monte Carlo problems are often much easier to formulate than the corresponding analytical problems [17]. As a consequence, fewer assumptions and simplifications are typically required, resulting in a more general and accurate model. To get an accurate estimate of the quantity of interest, the algorithm has to account for the physical or mathematical characteristics of the system in enough details. Furthermore, at each stage of sampling, the random numbers that are assigned to one or more of the variables need to follow the correct probability distributions. The accuracy of the estimate can be improved simply by increasing the number of samples N [17]. The standard deviation of the mean of the estimate diminishes always as $1/\sqrt{N}$.

The major drawback of the Monte Carlo method is its speed. Statistical sampling techniques that would today be labeled under Monte Carlo had been developed long before the 1940s [19]. Still, it stands to reason that the method got its name only at the dawn of electrical computing, as Monte Carlo algorithms are computationally very demanding as compared to most deterministic algorithms. The inventors of the Monte Carlo method had access to the only electronic computer in existence, ENIAC (Electronic Numerical Integrator And Computer) [20]. The 27 ton machine occupied roughly 170 m^2 of floor space, contained close to 18 000 vacuum tubes, consumed approximately 150 kW of power, and was by far the fastest calculator in the world [21]. Without ENIAC, meaningful Monte Carlo simulations would simply not have been feasible. Fortunately, the relative slowness of the Monte Carlo algorithms is much less of a problem today: a calculation that would have taken ENIAC 100 years to complete, can be solved in less than 5 minutes with a modern home computer.

The Monte Carlo method was first used to study neutron chain reactions in fissionable material. At the first stage of the simulation, a neutron was assigned a random position and velocity. The distance to the first collision site was determined by a random number whose probability distribution mirrored the distribution of the free paths of the neutron in the given material. The probabilities determined whether scattering, absorption or fission occurred. If, for example, the neutron was scattered as a result of the collision, a new propagation velocity (speed and direction) was determined by a random number whose probability distribution was defined by the characteristics of the system. The behavior of the corresponding physical system, such as the neutron multiplication rate, could be estimated by tracing the paths of multiple neutrons in this manner. [17, 18, 19]

In this thesis, Monte Carlo method is used to trace photons as they propagate inside the diffuser material. Incidentally, the basic structure of the model is very similar to that of the neutron chain reaction model fed to ENIAC back in late 1940s.

4.2 Technical details of the software

The graphical user interface of the software, shown in Figure 15, was written in *Python*. *Numpy* [22] and *Matplotlib* [23] were used for array handling and data plotting, respectively. The Monte Carlo algorithm was implemented in *Cython* [24] which allows users to compile fast C extensions from a Python code with minimal modifications. During a typical simulation run, roughly one hundred billion random numbers – equivalent to 800 GB of double precision floating point numbers – were drawn, necessitating a very fast pseudo-random number generator (RNG). An improved version of the popular and high-quality *Mersenne Twister* algorithm [25], namely *SIMD-oriented Fast Mersenne Twister (SFMT)* [26], was chosen for this purpose.

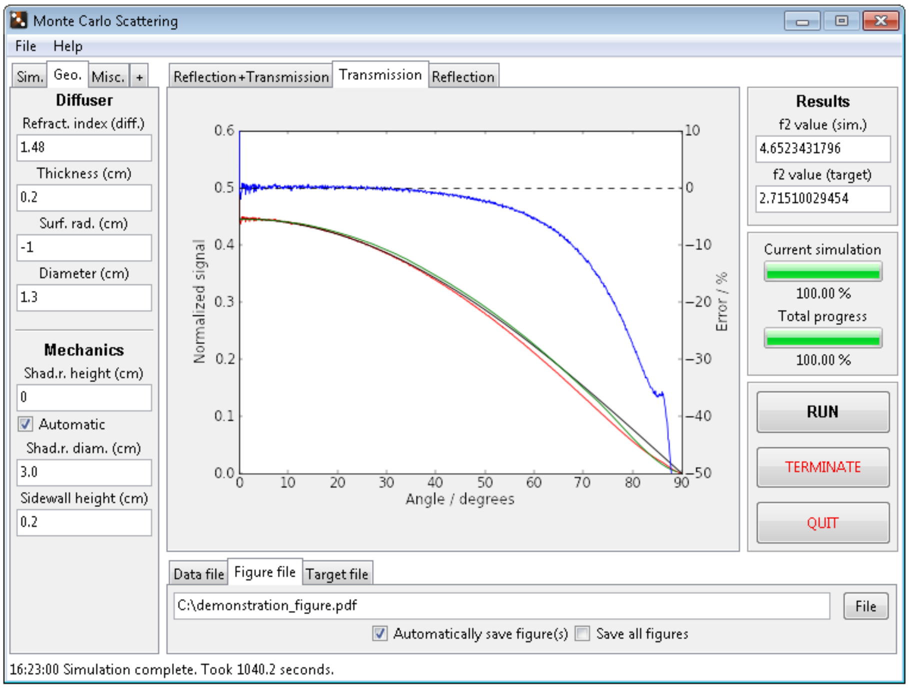

Refract. index (diff.) 1.48

Thickness (cm) 0.2

Surf. rad. (cm) -1

Diameter (cm) 1.3

Shad.r. height (cm) 0

☑ Automatic

Shad.r. diam. (cm) 3.0

Sidewall height (cm) 0.2

f2 value (sim.) 4.6523431796

f2 value (target) 2.71510029454

Current simulation 100.00 %

Total progress 100.00 %

C:\demonstration_figure.pdf

☑ Automatically save figure(s) ☐ Save all figures

16:23:00 Simulation complete. Took 1040.2 seconds.

Figure 15: Graphical user interface of the simulation software.

The simulation software is multi-threaded and the calculation work can be distributed to multiple processor cores. A typical simulation of one billion particles took roughly 10 and 15 minutes to complete on Intel i5-2500K quad core processor. Single simulations as well as parameter sweeps can be performed. Simulations can also be queued. The plotted figures can be saved in various formats, including PDF, SVG, PNG and TIFF. The raw data is stored to a text file for further analysis.

4.3 Detector structure

The structure of the detector assumed by the simulation software is shown in Figure 16, along with the various diffuser parameters that can be adjusted. Different diffuser shapes can be implemented in the software with relative ease. In this thesis, however, the study was limited to flat and spherically shaped diffusers. The distance of the detector to the diffuser together with the clear area of the diffuser determine the acceptance angle of the detector. The sidewalls of the diffuser housing, the shadow ring and the protective weather dome all have an effect on the angular response of the detector, as will be discussed shortly, and need therefore be accounted for in the simulations.

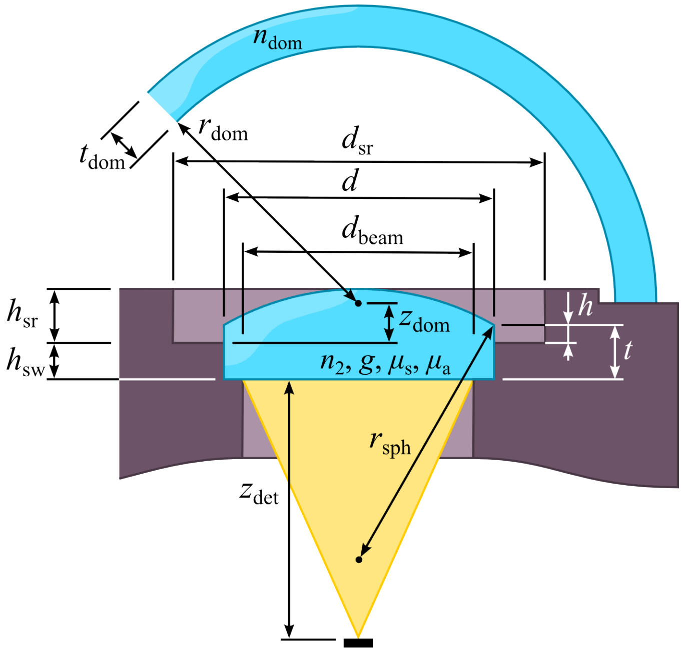

Figure 16: The detector geometry assumed by the simulation software. For explanation of the symbols, see the text.

While all of the parameters listed in Figure 16 can be changed in the simulation software, in reality, only a few of them can be adjusted freely. The refractive index of the diffuser n_2, the anisotropy parameter g, the scattering coefficient μ_{s}, and the absorption coefficient μ_{a} as well as the refractive index of the weather dome n_{dom} are all determined by material choices. The use of an existing weather dome design is typically preferred over designing new ones due to the production costs. Therefore, in practice, the thickness t_{dom} and the inner radius r_{dom} of the weather dome are determined by the dimensions of the existing domes. The offset of the weather dome z_{dom} relative to the front surface of the detector housing can be adjusted to some extent, but this has very little effect on the angular response of the detector. The distance between the detector and the diffuser z_{det} is governed by the mechanics of the detector head.

The most important parameters in diffuser optimization are the diameter d, the thickness t, and the height $h = t - h_{\mathrm{sw}}$ of the diffuser; the radius of curvature of the spherical front surface of the diffuser r_{sph}; the height of the sidewall h_{sw}; the diameter d_{sr}, and the height h_{sr} of the shadow ring; as well as the diameter of the clear area of the diffuser d_{beam}.

4.4 Simulation flow

The software uses 3D Monte Carlo particle tracing to simulate light transport in the diffuser structure. The algorithm is based on the framework laid out in the article by L. Wang et al. [28] that focuses on modeling light transport in multi-layer tissues. A more detailed description of the tissue simulation software is given in [29]. A short description of the working principles of the diffuser simulation software is given in this section, with emphasis on the aspects that differ from Wang's implementation.

While tracing photons from the sky towards the detectors would make sense from the physical point of view, the simulation performance would be very poor, since the vast majority of the photons incident upon the diffuser do not end up on the detector and therefore do not contribute to the overall angular response at all. For this reason, the photons are traced in the reverse direction, i.e. from the detector towards the sky. Moreover, instead of individual photons, large groups of particles are considered to allow for the partial absorption and refraction of the carried energy. This variance reduction technique is commonly used in photon and neutron simulations alike [19]. In the following discussion, these groups of particles traveling in the opposite direction to the actual photons are referred to simply as "particles".

The basic work flow of the diffuser simulation is illustrated in Figure 17. A particle emanates from the photodetector or the optical fiber and hits the air–diffuser interface at a random angle. Refraction alters the propagation direction, while a portion of the weight of the particle W – proportional to the energy of the particle – is lost in reflection.

Inside the diffuser, the particle can propagate, scatter and be absorbed. Upon reaching a diffuser–air interface, a portion of the particle weight is reflected and the rest is transmitted. If the transmitted particle hits the sidewall of the detector housing or the shadow ring, it is absorbed. The effect of the weather dome on the direction of propagation and the weight of the particle is also considered. The direction and the weight of the transmitted particle are stored in the system memory. The reflected particle, on the other hand, continues to propagate inside the diffuser.

When the particle weight has decreased – due to absorption and transmission – below a user-set threshold value, the propagation will end in a termination roulette.

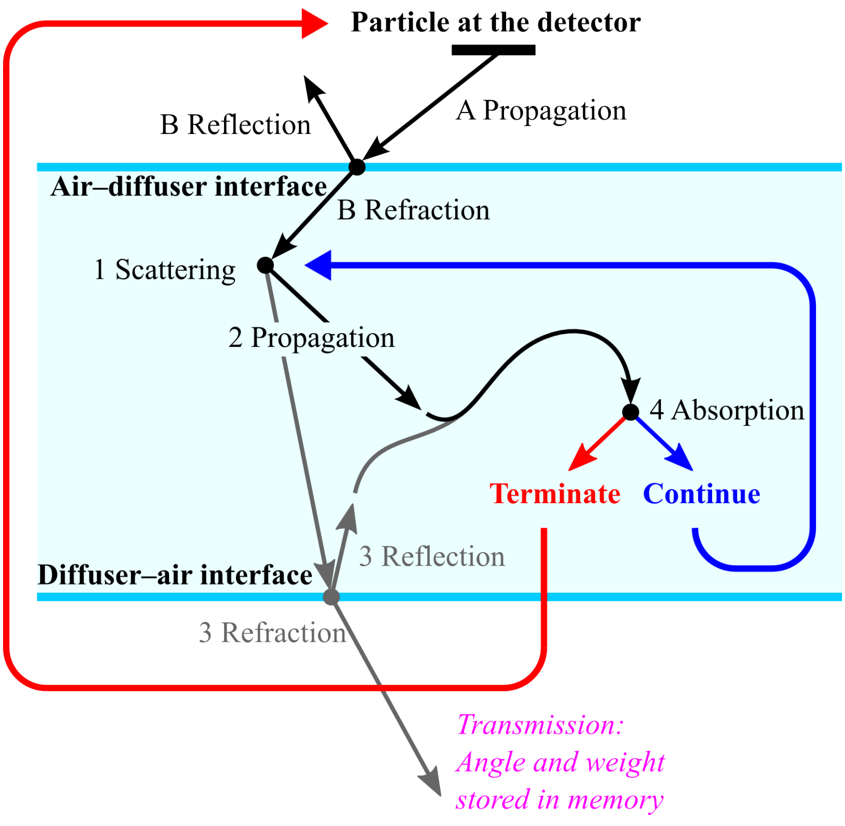

Figure 17: Work flow of the simulation process.

The entire process is repeated again and again for new particles until the angular response can be resolved with accuracy high enough.

4.5 Propagation and absorption

In Wang's light transport analysis [28], the absorption coefficient μ_{a} and the scattering coefficient μ_{s} are defined as the probabilities of particle absorption and scattering per unit pathlength, respectively. Thus, the higher the value of $\mu_{\mathrm{a}} + \mu_{\mathrm{s}}$, the shorter the average pathlength between two collisions. The step size s of the particle can be derived [18, 28] from the definitions of μ_{a} and μ_{s}, as

$$s = -\frac{\ln(\chi)}{\mu_{\mathrm{a}} + \mu_{\mathrm{s}}} \,, \tag{3}$$

where χ is a uniformly distributed random number in the interval (0,1). The mean free path between the interaction sites, scattering or absorption, is

$$\langle s \rangle = \frac{1}{\mu_{\mathrm{a}} + \mu_{\mathrm{s}}} \,. \tag{4}$$

After the step size s has been determined, the position of the particle is updated by setting

$$\begin{cases} x \leftarrow x + \mu_{\mathrm{x}} s \\ y \leftarrow y + \mu_{\mathrm{y}} s \\ z \leftarrow z + \mu_{\mathrm{z}} s \end{cases} , \tag{5}$$

provided that the particle does not encounter a material interface before it reaches the end point. In the equation, x, y, and z are the particle coordinates and μ_{x}, μ_{y}, and μ_{z} are the corresponding directional cosines, for which it holds

$$\mu_{\mathrm{x}}^2 + \mu_{\mathrm{y}}^2 + \mu_{\mathrm{z}}^2 = 1 \ . \tag{6}$$

The particle weight is initially $W = 1$. As the particle propagates, it loses some of its weight due to absorption. The change in particle weight ΔW after each propagation step, is calculated as

$$\Delta W = -\frac{\mu_{\mathrm{a}}}{\mu_{\mathrm{s}}} W \ . \tag{7}$$

Here, the absorption coefficient μ_{a} is is assumed to be smaller than the scattering coefficient μ_{s}, as is the case with all practical diffuser materials. The weight of the particle is updated through the substitution $W \leftarrow W + \Delta W$. [28]

As the particle loses more and more of its weight, its potential contribution to the angular response becomes smaller and smaller. To maintain simulation efficiency, the particle is terminated when its weight is below a given threshold value W_{th}. In typical simulations, a threshold value of $W_{\mathrm{th}} = 0.0001$ was used.

To conserve energy during the termination process, a termination roulette technique is utilized [28]. Below the termination threshold, the particle weight either goes to zero or is multiplied by the roulette parameter m according to

$$W \leftarrow \begin{cases} mW, & \text{if } \chi \leq 1/m \\ 0, & \text{if } \chi > 1/m \end{cases} , \tag{8}$$

where χ is a uniformly distributed random number in the interval [0,1). If the particle survives the termination roulette, it continues to propagate. In the simulations, the roulette parameter was set to $m = 10$.

4.6 Scattering

The scattering probability per unit pathlength is determined by the scattering coefficient μ_s. After each propagation and absorption step, the particle is scattered. The deflection angle α relative to the initial propagation direction – shown in Figure 18(a) – is governed by Henyey–Greenstein scattering phase function

$$\phi(\alpha) = \frac{1}{4\pi} \frac{1 - g^2}{(1 + g^2 - 2g\cos(\alpha))^{3/2}} \, , \tag{9}$$

where $-1 \leq g \leq 1$ is the scattering anisotropy parameter. When $g = 0$, the scattering is isotropic and the particle is equally likely to travel in any direction. Negative values of g indicate backward directed scattering whereas positive values correspond to forward directed scattering. [27] In Figure 18(b), the scattering phase function of equation (9) is plotted as a function of the deflection angle α at four values of g.

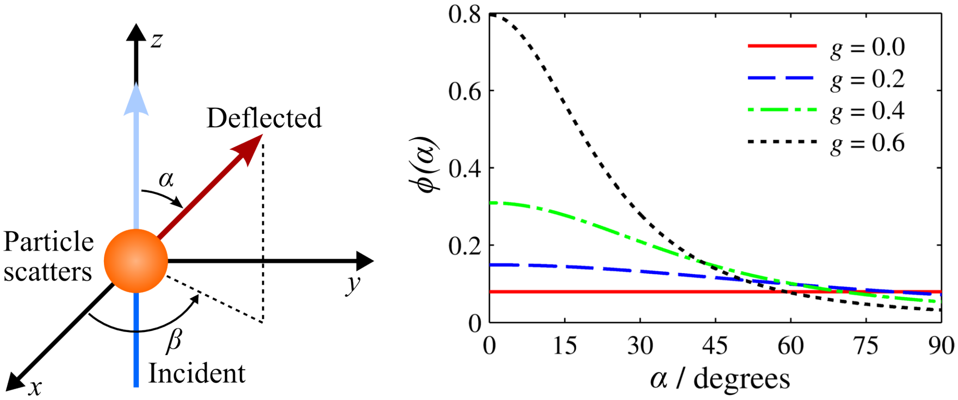

(a) (b)

Figure 18: The scattering process is illustrated in (a), where α and β correspond to deflection and azimuth angles, respectively. In (b), Henyey–Greenstein phase function of (9) is plotted at different values of the anisotropy parameter g.

As noted by A. Witt [30], the cosine of the deflection angle can be calculated efficiently from the equation

$$\cos(\alpha) = \begin{cases} 2\chi - 1, & \text{if } g = 0 \\ \frac{1}{2g}\left[1 + g^2 - \left(\frac{1-g^2}{1-g+2g\,\chi}\right)^2\right] & \text{if } g \neq 0 \end{cases} \, , \tag{10}$$

where χ is a random number in the interval [0,1). The azimuthal scattering angle

β, on the other hand, is always calculated as

$$\beta = 2\pi\chi \ , \tag{11}$$

where the result is expressed in radians [28].

The new directional cosines can be calculated from

$$\begin{cases} \mu_\mathrm{x} \leftarrow \frac{\sin(\alpha)}{\sqrt{1-\mu_\mathrm{z}^2}} \left[\mu_\mathrm{x}\mu_\mathrm{z}\cos(\beta) - \mu_\mathrm{y}\sin(\beta)\right] + \mu_\mathrm{x}\cos(\alpha) \\ \mu_\mathrm{y} \leftarrow \frac{\sin(\alpha)}{\sqrt{1-\mu_\mathrm{z}^2}} \left[\mu_\mathrm{y}\mu_\mathrm{z}\cos(\beta) + \mu_\mathrm{x}\sin(\beta)\right] + \mu_\mathrm{y}\cos(\alpha) \\ \mu_\mathrm{z} \leftarrow -\sin(\alpha)\cos(\beta)\sqrt{1-\mu_\mathrm{z}^2} + \mu_\mathrm{z}\cos(\alpha) \end{cases} . \tag{12}$$

If $|\mu_\mathrm{z}| = 1$, the following form should be used instead

$$\begin{cases} \mu_x \leftarrow \sin(\alpha)\cos(\beta) \\ \mu_y \leftarrow \sin(\alpha)\sin(\beta) \\ \mu_z \leftarrow \mathrm{sgn}(\mu_\mathrm{z})\cos(\alpha) \end{cases} , \tag{13}$$

where sgn is the sign, or signum, function [28].

4.7 Reflection and refraction

In Wang's software for analyzing light transport in tissues [29], the sample was assumed to consist of one or multiple flat, semi-infinite sheets of material. When simulating light propagation in diffusers, the same assumption cannot be made. Not only does the diffuser have a finite diameter, but the front surface of the diffuser may also be non-flat. Reflection and refraction of light at the surfaces of the diffuser affect the overall angular response considerably. Therefore, special attention needs to be paid to these interface effects.

In order to calculate the angles of reflection and refraction, one must first find out the coordinates $(x_\mathrm{s}, y_\mathrm{s}, z_\mathrm{s})$ at which the particle crosses the material interface. In addition, the surface normal vector $\tilde{\mathbf{n}}$ at these coordinates must be known.

The distance s_sph to the spherical front surface of the diffuser (centered at $(0, 0, z_\mathrm{sph})$, radius of curvature r_sph) for a particle that is located at (x, y, z) and that is moving in the direction set by $(\mu_\mathrm{x}, \mu_\mathrm{y}, \mu_\mathrm{z})$ can be determined by solving the quadratic equation

$$(x + \mu_\mathrm{x} s_\mathrm{sph})^2 + (y + \mu_\mathrm{y} s_\mathrm{sph})^2 + (z + \mu_\mathrm{z} s_\mathrm{sph} - z_\mathrm{sph})^2 = r_\mathrm{sph}^2 \ . \tag{14}$$

The equation generally has two solutions. However, noting that the initial coordinates (x, y, z) always lie within the sphere and that the distance to travel needs to be positive ($s_{\mathrm{sph}} > 0$), the only possible solution is

$$s_{\mathrm{sph}} = \frac{-b + \sqrt{b^2 - ac}}{a} \qquad \begin{cases} a = \mu_{\mathrm{x}}^2 + \mu_{\mathrm{y}}^2 + \mu_{\mathrm{z}}^2 \\ b = x\mu_{\mathrm{x}} + y\mu_{\mathrm{y}} + (z - z_{\mathrm{sph}})\mu_{\mathrm{z}} \\ c = x^2 + y^2 + (z - z_{\mathrm{sph}})^2 - r_{\mathrm{sph}}^2 \end{cases} \tag{15}$$

Similarly, the distance s_{sw} to the diffuser sidewall – or its extension – is

$$s_{\mathrm{sw}} = \frac{-(x\mu_{\mathrm{x}} + y\mu_{\mathrm{y}}) + \sqrt{(x\mu_{\mathrm{x}} + y\mu_{\mathrm{y}})^2 - (\mu_{\mathrm{x}}^2 + \mu_{\mathrm{y}}^2)(x^2 - y^2 - r^2)}}{\mu_{\mathrm{x}}^2 + \mu_{\mathrm{y}}^2} , \tag{16}$$

where $r = d/2$ is the radius of the diffuser disk. The distance to the flat facet of the diffuser is simply

$$s_{\mathrm{f},i} = \frac{z_{\mathrm{f},i} - z}{\mu_{\mathrm{z}}} \quad i = 1, 2 \tag{17}$$

where $z_{\mathrm{f},1}$ and $z_{\mathrm{f},2}$ detonate the z coordinates of the front and the back surfaces of the diffuser. Distance s_1 is relevant only in the absence of a spherical front surface.

If the step size s is larger than the smallest of the positive distances s_{min} of (15)–(17), partial reflection occurs. The coordinates $(x_{\mathrm{s}}, y_{\mathrm{s}}, z_{\mathrm{s}})$ at which the particle crosses the material interface can be calculated from (5) by replacing s with the distance to the interface s_{min}. The surface normal vectors $\tilde{\mathbf{n}}$ for spherical front surface, cylindrical sidewall, and the flat end facet(s), respectively, are

$$\tilde{\mathbf{n}}_{\mathbf{sph}} = -\frac{1}{r_{\mathrm{sph}}} \begin{bmatrix} x_{\mathrm{s}} \\ y_{\mathrm{s}} \\ z_{\mathrm{s}} - z_{\mathrm{sph}} \end{bmatrix} , \qquad \tilde{\mathbf{n}}_{\mathbf{sw}} = -\frac{1}{r} \begin{bmatrix} x_{\mathrm{s}} \\ y_{\mathrm{s}} \\ 0 \end{bmatrix} , \qquad \tilde{\mathbf{n}}_{\mathbf{f,i}} = \mp \begin{bmatrix} 0 \\ 0 \\ 1 \end{bmatrix} . \tag{18}$$

The reflection and refraction on the surface of a sphere is illustrated in Figure 19. The directional cosine vectors of reflection $\tilde{\mathbf{s}}_{\mathbf{reflect}}$ and refraction $\tilde{\mathbf{s}}_{\mathbf{refract}}$ are

$$\begin{aligned} \tilde{\mathbf{s}}_{\mathbf{reflect}} &= \tilde{\mathbf{s}}_{\mathbf{incident}} + 2\cos(\nu_1)\tilde{\mathbf{n}} \text{ , and} \qquad (19) \\ \tilde{\mathbf{s}}_{\mathbf{refract}} &= \frac{n_1}{n_2}\tilde{\mathbf{s}}_{\mathbf{incident}} + \left(\frac{n_1}{n_2}\cos(\nu_1) - \cos(\nu_2)\right)\tilde{\mathbf{n}} \text{ ,} \qquad (20) \end{aligned}$$

where $\tilde{\mathbf{s}}_{\mathbf{incident}} = [\mu_{\mathrm{x}}\, \mu_{\mathrm{y}}\, \mu_{\mathrm{z}}]$ is the incident directional cosine vector, and n_1 and n_2 are the refractive indices of the first and the second material, respectively. [31] The incident and refraction angles ν_1 and ν_2 can be solved from the equations

$$\cos(\nu_1) = -\tilde{\mathbf{n}} \cdot \tilde{\mathbf{s}}_{\mathbf{incident}} \ , \quad \text{and} \tag{21}$$

$$n_1 \sin(\nu_1) = n_2 \sin(\nu_2) \ , \tag{22}$$

where $\tilde{\mathbf{x}} \cdot \tilde{\mathbf{y}}$ is the dot product between the two vectors.

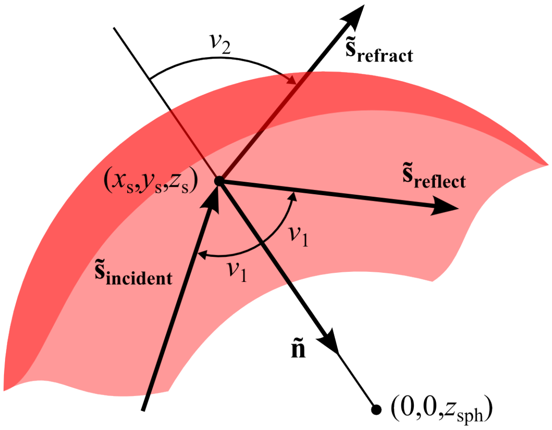

Figure 19: Reflection and refraction of light on the inner surface of a sphere.

Below the angle of total internal reflection $[\nu_1 < \sin^{-1}(n_2/n_1)]$ the reflectance R and the transmittance T at the material interface are calculated as

$$R = \frac{1}{2}\left[\frac{\sin^2(\nu_1 - \nu_2)}{\sin^2(\nu_1 + \nu_2)} + \frac{\tan^2(\nu_1 - \nu_2)}{\tan^2(\nu_1 + \nu_2)}\right] \ , \quad \text{and} \tag{23}$$

$$T = 1 - R \ , \tag{24}$$

assuming that the light is unpolarized. If the incident angle is higher than the angle of the total internal reflection, the transmittance is $T = 0$. [28, 32] After the collision, the weight of the reflected particle is set to $W \leftarrow R \cdot W$. The directional cosine vector is updated ($\tilde{\mathbf{s}}_{\mathbf{incident}} \leftarrow \tilde{\mathbf{s}}_{\mathbf{reflect}}$) and the reflected particle travels the remaining distance $s - s_{\min}$ in the new direction, unless new reflections occur.

The weight of the transmitted particle is $T \cdot W$, where W is the weight of the particle before the reflection and the refraction. Transmitted particles traveling towards the detector ($\mu_z < 0$) are ignored. If the particle hits either the sidewall of the diffuser or the shadow ring, its weight is absorbed. If present, the weather dome will alter the angle and the weight of the particle slightly, as will be discussed shortly. Finally, the zenith angle $\cos^{-1}(\mu_z)$ and the weight of the transmitted particle are stored in the memory.

4.8 Weather dome

The weather dome is a hollow quartz hemisphere whose inner radius is r_{dom} and thickness is t_{dom} (see Figure 16). Light is reflected at both the inner and the outer surfaces of the sphere. At each interface, the reflection and the refraction angles can be determined from equations (20) through (22). Similarly, the reflectances and the transmittances can be calculated from (23) and (24), respectively.

As illustrated in Figure 20, the particles are continuously reflected between the two surfaces of the weather dome. Calculating the directional cosines as well as the reflectances and the transmittances repeatedly would be needlessly time consuming, as by far the largest contribution to the total reflected and transmitted power comes from the first reflected and transmitted components. To increase simulation efficiency, the dome is approximated as a flat sheet of material and the total transmittance is calculated from a geometrical series as

$$\begin{aligned} T_{\text{tot}} &= T_{\text{in}}T_{\text{out}} + T_{\text{in}}R_{\text{out}}R_{\text{in}}T_{\text{out}} + T_{\text{in}}(R_{\text{out}}R_{\text{in}})^2T_{\text{out}} + \cdots \\ &= T_{\text{in}}T_{\text{out}}\sum_{i=0}^{\infty}(R_{\text{out}}R_{\text{in}})^i = \frac{T_{\text{in}}T_{\text{out}}}{1-R_{\text{out}}R_{\text{in}}} \ , \end{aligned} \tag{25}$$

where T_{in}, T_{out}, R_{in}, and R_{out} are the transmittances and the reflectances at the inner and outer surfaces of the weather dome, respectively. These values were approximated by the ones calculated from the first two material interfaces of the dome, i.e. the values $T_{\text{in},1}$, $T_{\text{out},1}$, $R_{\text{in},1}$, and $R_{\text{out},1}$ in Figure 20. The material is assumed to be non-absorbing. Hence, the total reflectance is $R_{\text{tot}} = 1 - T_{\text{tot}}$. All transmitted particles are assumed to travel in the direction of the first component that is transmitted through both material interfaces. Similarly, the propagation direction of the reflected particles is determined by the first reflection from the inner surface of the weather dome.

While the curvatures of the two surfaces of the weather dome affect the results to some extent, the flat sheet approximation is still reasonably accurate in typical applications for various reasons. First, the incident angle with respect to the surface normal of the weather dome is typically relatively small (see Figure 20) and the particles do not travel long distances along the weather dome when they reflect back and forth between the two material interfaces. Second, the thickness of the weather dome is quite small as compared to its radius and the difference in the inner and outer wall curvatures is negligible.

Based on equations (23), (24), and (25), approximately 7.7 % of the particle

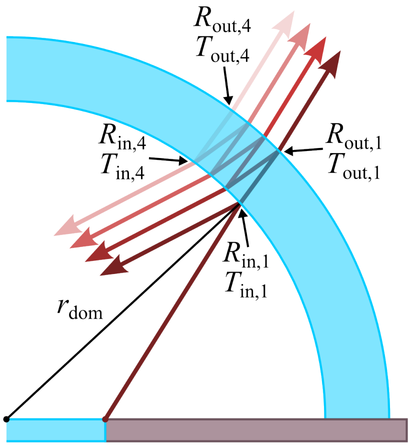

Figure 20: Multiple reflections inside the quartz dome. The thickness of the dome has been greatly exaggerated for illustration purposes.

weight is reflected from the weather dome, assuming normal incidence and refractive index of 1.5. The reflected particles can contribute to the overall angular response, provided that they are traveling in the forward direction ($\mu_z \geq 0$). Particles that are reflected back to the diffuser are ignored because their contribution to the overall angular response is expected to be small. The second reflection from the inner surface of the weather dome is ignored for the same reason.

5 Simulation results

Results of the diffuser performance simulations are presented in this section. First, the measured and simulated angular responses for raised diffusers are compared. Next, the effects of different parameters of the diffuser on the overall performance are discussed. Finally, the optimal designs for two detector heads, one with raised flat diffuser and the other with shaped diffuser, are presented.

5.1 Measured and simulated angular responses

In Section 3, Quartz C was found to be the most suitable material for the improved solar UV diffuser. Therefore, it was selected as the base material for the simulations. The simulated results were matched with the results of the measurements described in Section 3 by tuning the scattering coefficient μ_s. Scattering dominated over absorption ($\mu_\mathrm{s} \gg \mu_\mathrm{a}$). The assumption of uniform scattering ($g = 0$) turned out to yield the best results for Quartz C. A value of $n_2 = 1.5$ was used for the refractive index of the diffuser. The diameter and the thickness of the diffuser were $d = 15$ mm and $t = 2$ mm, respectively. The diameter of the clear area of the diffuser in the prototype detector was $d_\mathrm{beam} = 13$ mm. Weather dome was used in neither the measurements nor the simulations.

To validate the correct operation of the simulation software, the diffuser was raised first 1 mm and then 2 mm relative to the detector surface in both the simulation, and the measurements setup. The shadow ring was in level with the front surface of the diffuser in each measurement and simulation. The diameter of the shadow ring was $d_\mathrm{sr} = 27$ mm. Figure 21 shows good agreement between the measured and simulated angular responses in all three cases, suggesting that the software can indeed be used to optimize diffuser designs.

The optimal height of the diffuser in the prototype detector configuration was approximately $h = 1$ mm, as can be deduced from Figure 21. The integrated cosine error calculated from the measurement results using equation (2) was $f_2 = 2.3$ % at this height. It is evident that significant portion of the signal is ”missing” at large zenith angles, resulting in large relative deviations from the cosine response. To improve the angular response of the detector further, more prominent changes in the detector configuration, such as altering the diameter of the the diffuser or shaping its front surface, are required.

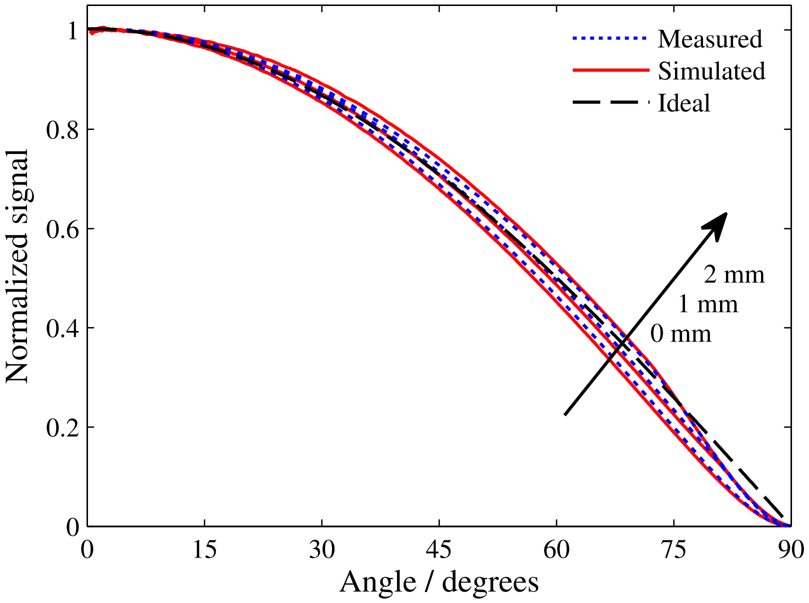

Figure 21: Comparison between measured (dotted blue line) and simulated (solid red line) angular responses at three different diffuser heights $h = 0$ mm, 1 mm, and 2 mm. Also plotted is the ideal cosine response (dashed black line).

5.2 Effects of various parameters on the angular response

5.2.1 Refractive index

Figure 22 illustrates the effect of the refractive index of the diffuser material on the overall angular response. A flat diffuser sheet of a very large diameter d was used in the simulations in order to eliminate the effect of the shape of the diffuser on the angular response. The particles hit the center of the diffuser at normal incidence. Uniform scattering ($g = 0$) was assumed. The scattering coefficient μ_s was set to a very high value, which meant that only a very small portion of the radiation was transmitted by the diffuser. Therefore, the particles were collected at the reflection side of the diffuser in these simulations.

The angular response of a volume diffuser deviates significantly from a cosine function even if it has ”ideal” properties, i.e. no scattering anisotropy ($g = 0$) and high scattering probability per unit pathlength (large μ_s). This is caused by the refractive index difference between the diffuser and the surrounding medium, which not only affects the angle of the transmitted particle – equation (22) – but also the transmittance through the material interface – equation (24). Similar non-Lambertian behavior has previously been reported in fluorescent materials [33]. The

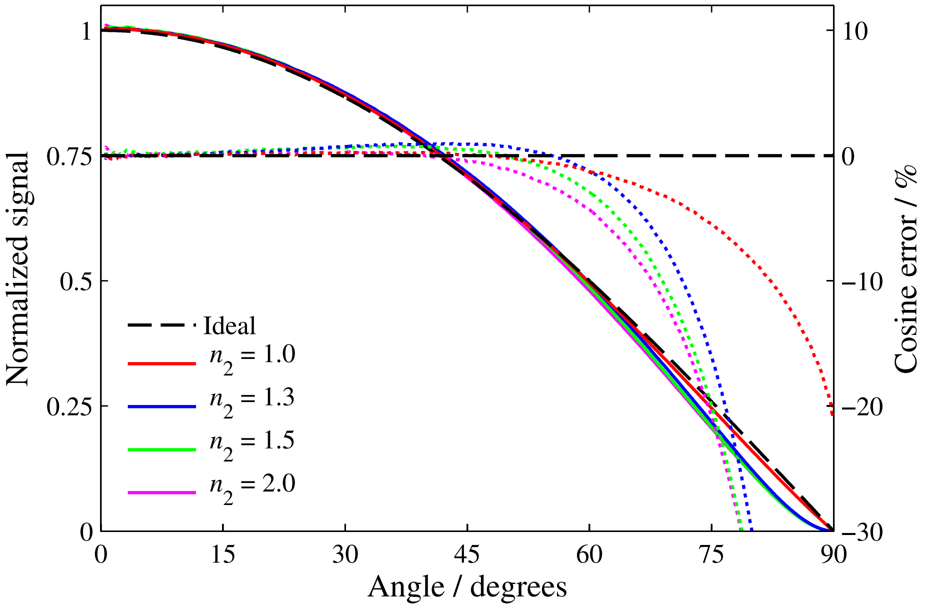

Figure 22: Simulated angular response of the diffuser at various values of the refractive index of the material. Due to small penetration depth of the material, reflected, as opposed to transmitted, particles are considered in these simulations. Also plotted is the ideal cosine response (dashed black line).

finding indicates that perfect cosine response simply cannot be achieved without compensating for the effects of the refractive index difference in one way or the other. In practice, this is done by altering the shape of the diffuser.

As seen in Figure 22, even the angular response of a diffuser whose refractive index is unity deviates from the ideal cosine response at large zenith angles. This can at least partially be explained by the fact that a particle incident on the material interface at a large angle has to travel a long distance inside the material, and is therefore more likely to scatter again before reaching the surface of the diffuser.

5.2.2 Diffuser dimensions

The effect of diffuser height on the angular response was already illustrated in Figure 21: the sidewalls affect the shape of the response more and more, as the diffuser is raised. The diameter of the diffuser d determines the area-to-volume ratio as well as the sidewall-to-facet area ratio of the structure. Therefore, altering the diameter of the diffuser affects the overall angular response of the detector considerably. This is demonstrated in Figure 23 where the angular response of a detector with a raised diffuser has been plotted at four diffuser diameters $d = 10$ mm, 15 mm, 20 mm and 25 mm. The thickness and the height of the diffuser were $t = 2$ mm and $h = 1$ mm, respectively. The separation between the shadow ring and the diffuser was kept at 5 mm throughout all the simulations. Similarly, the difference in the diameter between the diffuser itself and the area of the diffuser visible to the detector was $d - d_{\mathrm{beam}} = 2$ mm in all cases. For reference, the angular response of an "infinite" diffuser with no transmission through the sidewalls is also plotted in Figure 23 as a red line.

It is evident that as the diameter increases, the transmission through the sidewalls of the diffuser affects the overall angular response less and less. This effect can cause problems in applications where large area diffusers are required, because in order to compensate for the poor angular response at large zenith angles, either the thickness of the diffuser needs to be increased considerably, or more complex diffuser geometries are required. The former technique would decrease the signal level considerably, as shown in Figure 10, while the latter would likely increase the manufacturing costs significantly as compared to simple raised flat diffuser designs.

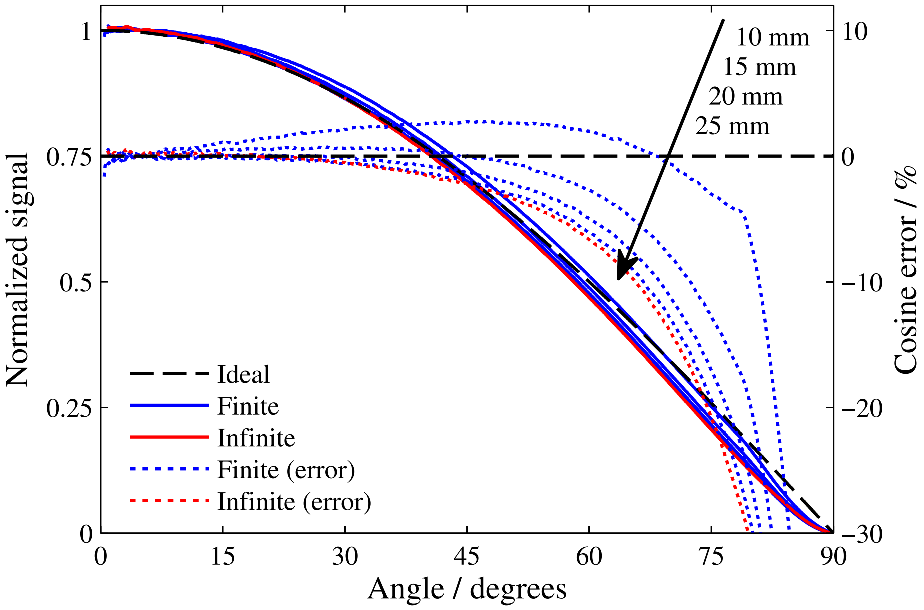

Figure 23: Simulated angular response of a detector at four different diameters of the diffuser (blue lines). The angular response of the detector with infinite sheet of diffuser material is shown as a red line. Also plotted is the ideal cosine response (dashed black line).

5.2.3 Diffuser curvature

The angular response of the detector can be altered considerably by shaping of the front surface of the diffuser. Figure 24 shows the simulated angular response of the detector at different radius of curvatures $r_{\mathrm{sph}} = 10$ mm, 20 mm, 30 mm, and 40 mm of the spherical front surface of the diffuser. The thickness at the edge of the diffuser was $t = 1$ mm and the height of the diffuser was $h = 0.5$ mm in all simulations. The diameter of the diffuser was kept at $d = 10$ mm. The diameter of the shadow ring was $d_{\mathrm{sr}} = 25$ mm, and it was aligned with the highest part of the diffuser – similar to Figure 16.

The possibility to shape the diffusers gives the designer more control over the overall angular response. Nevertheless, as is evident from the cosine error curves of Figure 24, careful design is still required to reach near-ideal cosine response. Large curvature of the front surface of the diffuser increases the angular response at high zenith angles. As the radius of curvature increases, the angular response approaches that of a flat diffuser (red line in Figure 24).

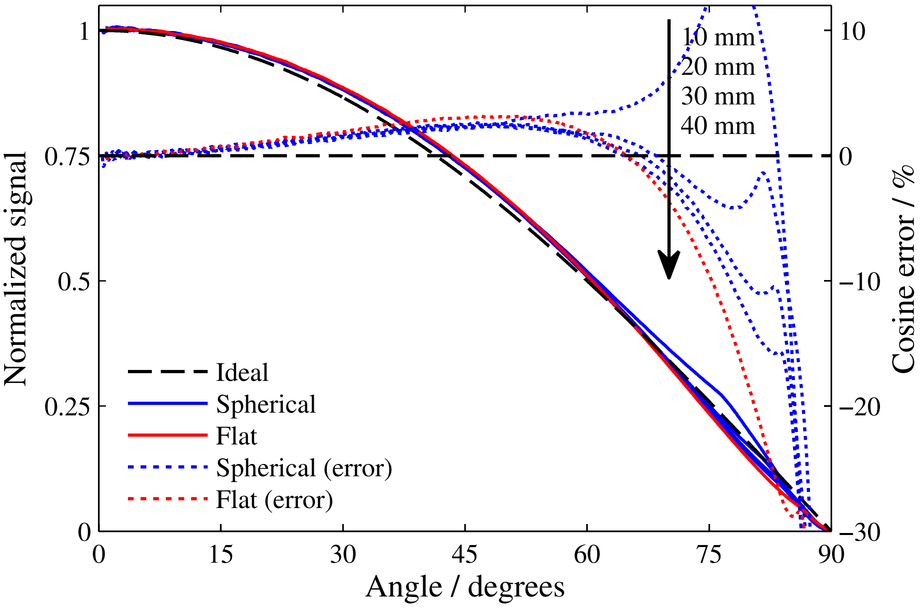

Figure 24: Simulated angular response of a detector at four different radius of curvatures of the spherical front surface. The angular response of a detector with a flat diffuser is shown as a red line. Also plotted is the ideal cosine response (dashed black line).

5.2.4 Shadow ring

The diameter and the height of the shadow ring both have a considerable effect on the angular response of the detector at large zenith angles. The angular responses of Figure 25 were obtained by varying the diameter of the shadow ring d_{sr} from 12.5 mm to 32.5 mm in the intervals of 5 mm. The diameter, the thickness, and the height of the flat diffuser were $d = 10$ mm, $t = 2$ mm, and $h = 1$ mm in all cases. For comparison, the angular response of a non-raised diffuser (green line) is also plotted in the figure. The responses correspond precisely to the angular response of the detector without a shadow ring (red line in Figure 25) until the angle θ_{sr} at which the shadow ring starts blocking the radiation. This turning point can be estimated as

$$\theta_{\mathrm{sr}} = 90^\circ - \tan^{-1}\left(\frac{2h}{d_{\mathrm{sr}} - d}\right) , \tag{26}$$

where d_{sr} is the diameter of the shadow ring, and d and h are the diameter and the height of the diffuser, respectively. With the shadow ring diameter of $d_{\mathrm{sr}} = 17.5$ mm, the equation yields $\theta_{\mathrm{sr}} = 75.1^\circ$, which is very close to the simulation value, i.e. the turning point of the second dotted blue line from the left in Figure 25.

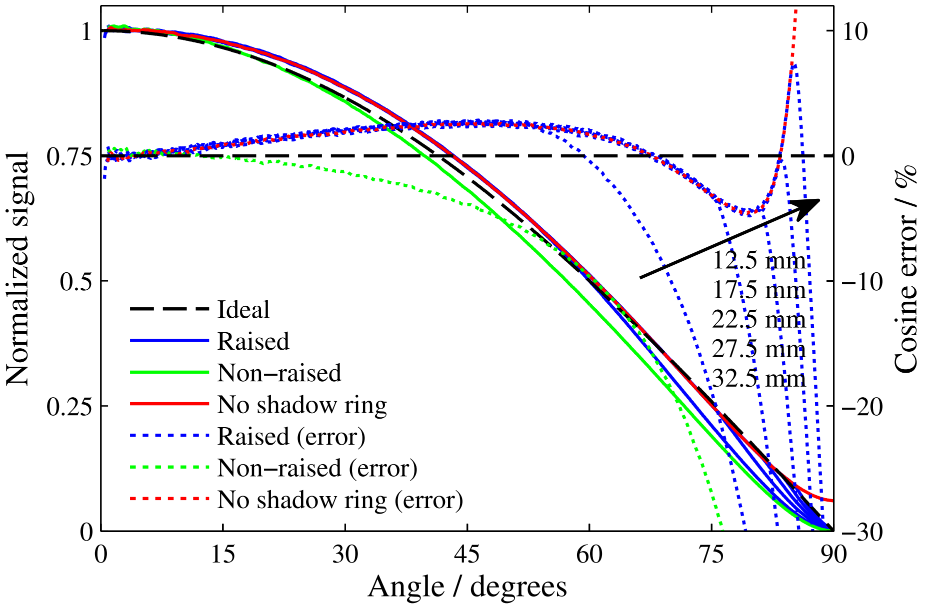

Figure 25: Simulated angular response of a detector at five different diameters of the shadow ring. The angular response of a detector with non-raised diffuser is shown as a green line whereas that of a detector without a shadow ring is shown as a red line. Also plotted is the ideal cosine response (dashed black line).

Interesting results can be obtained by slightly lowering the shadow ring relative to the front surface of the diffuser. In Figure 26, the angular response of a diffuser ($d = 10$ mm, $t = 2$ mm, and $h = 1$ mm) is plotted at different heights of the shadow ring h_{sr}, ranging from 0.5 mm to 1 mm (full shadow ring). The diameter of the shadow ring was set to $d_{\mathrm{sr}} = 27$ mm. While the angular response at small incident angles is unaltered, considerable improvements in the cosine response at very high angles can be obtained with this technique. The drawback is that some light will reach the diffuser at incident equal to and higher than 90°. The calculated integrated cosine error of the example detector with the full shadow ring is $f_2 = 1.79$ %. Lowering the shadow ring by 0.3 mm, the integrated cosine error can be decreased to $f_2 = 1.55$ %. This result also gives some indication about the sensitivity of the angular response and the integrated cosine error of equation (2) to variations in the parameter values.

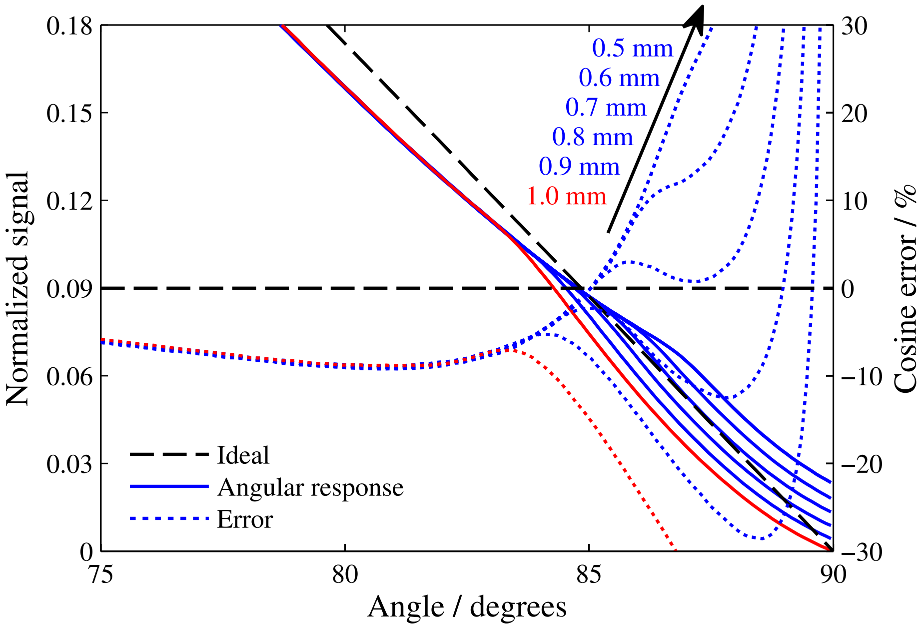

Figure 26: Simulated angular response of a detector at six different heights of the shadow ring. Red line corresponds to full shadow ring. Also plotted is the ideal cosine response (dashed black line).

5.2.5 Clear area of the diffuser

Figure 27 shows the angular response at different diameters of the visible area of the detector d_{beam}, ranging from 0 mm (point-like visible area) to 10 mm (diffuser fully visible). The distance between the detector and the diffuser was $z_{\mathrm{det}} = 29$ mm throughout all the simulations. The diameter, the thickness, and the height of the diffuser were $d = 10$ mm, $t = 2$ mm, and $h = 1$ mm, respectively. The diameter of the shadow ring was $d_{\mathrm{sr}} = 27$ mm. If only the center part of the raised diffuser is visible to the detector, then the edges of the diffuser will have relatively little effect on the overall angular response of the diffuser head. As the diameter of the visible area is increased, more and more of the light that is transmitted by the sidewalls of the diffusers will reach the detector.

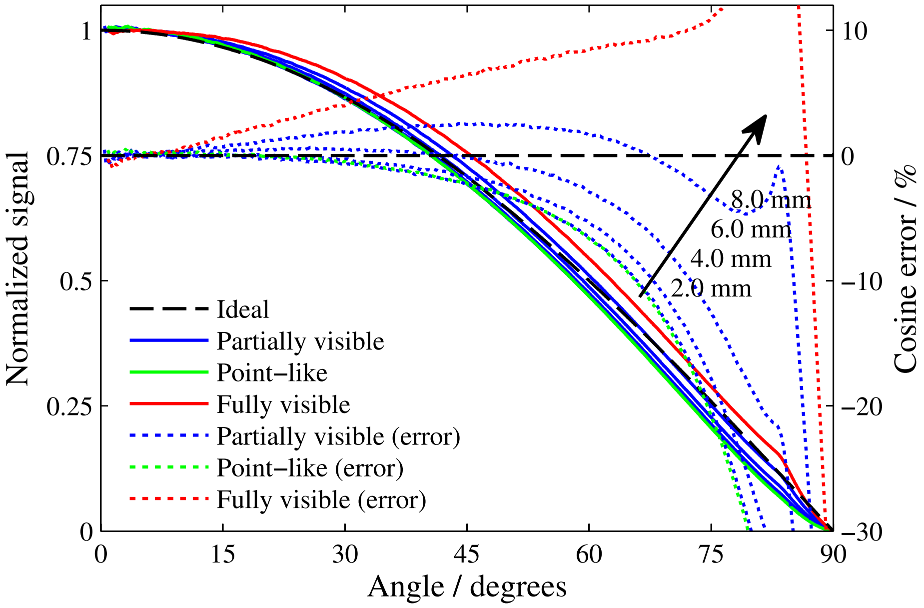

Figure 27: Simulated angular response of a detector at different diameters of the visible area of the diffuser. The angular response of a detector with fully visible diffuser is highlighted in red whereas that of a detector with zero diameter visible area is shown in green. Also plotted is the ideal cosine response (dashed black line).

Figure 27 also demonstrates the sensitivity of the angular response to variations in the size of the visible area of the detector. By comparing the topmost three cosine error curves of the figure – corresponding to visible area diameters of $d_{\mathrm{beam}} = 10$ mm, 8 mm, and 6 mm – it is evident that the angular response is very sensitive to variations in the parameter value when the diameter of the clear area d_{beam} is close to that of the diffuser d. The extreme sensitivity of the angular response – and consequently the integrated cosine error f_2 – to the size of the clear area of the diffuser has several implications on the diffuser design. First, the diameter of the clear area needs to be optimized carefully. Second, the visible area of the diffuser should be limited mechanically (as shown schematically in Figure 16) and not, for example, through the acceptance angle of the optical fiber. In the latter case, even a very small alignment error of the optical fiber would mean that the angular response was no longer independent of the azimuth angle of the incoming radiation. Finally, the incident angle dependence of the fiber/photodetector signal level needs to be taken into account when designing the diffuser head.

The angular response becomes considerably less sensitive to the diameter of the visible area as the value decreases. However, making the clear area of the diffuser significantly smaller than that of the diffuser itself is rarely a viable solution, because the poor angular response at large angles cannot be effectively compensated by raising the diffuser anymore.

5.2.6 Weather dome

As discussed in Section 4.8, the protective weather dome will affect the angular response of the detector head to some extent. Figure 28 shows the simulated angular response of one diffuser design with and without the weather dome. Three different weather dome radii $r_{\text{dom}} = 10$ mm, 15 mm, and 20 mm were studied. The thickness of the glass was $t_{\text{dom}} = 1.7$ mm. The diameter of the shadow ring was $d_{\text{sr}} = 27$ mm, while the diameter, the thickness, and the height of the diffuser were $d = 10$ mm, $t = 2$ mm, and $h = 1$ mm, respectively.

As can be seen in Figure 28, the shape of the angular response of the detector is only slightly altered by the weather dome. The integrated cosine errors of equation (2), were $f_2 = 1.75$ %, 1.86 %, and 1.88 % for weather dome radii $r_{\text{dom}} = 10$ mm, 15 mm, and 20 mm respectively. Integrated cosine error of the detector without a weather dome was $f_2 = 1.82$ %. The results suggest that, while the cosine response is affected by the weather dome, separate diffusers need not be designed for two detectors that differ only in their use of weather dome, provided that the diameter of the weather dome is large enough as compared to that of the diffuser. If on the other hand, the diffuser and the dome are of similar diameter, the effect of the weather dome on the angular response needs to be taken into account in the design process.

5.3 Diffuser optimization

5.3.1 Optimization process

Finding the optimal value of any one of the diffuser parameters is a simple process: a decent initial guess and a relatively short parameter sweep will suffice. However,

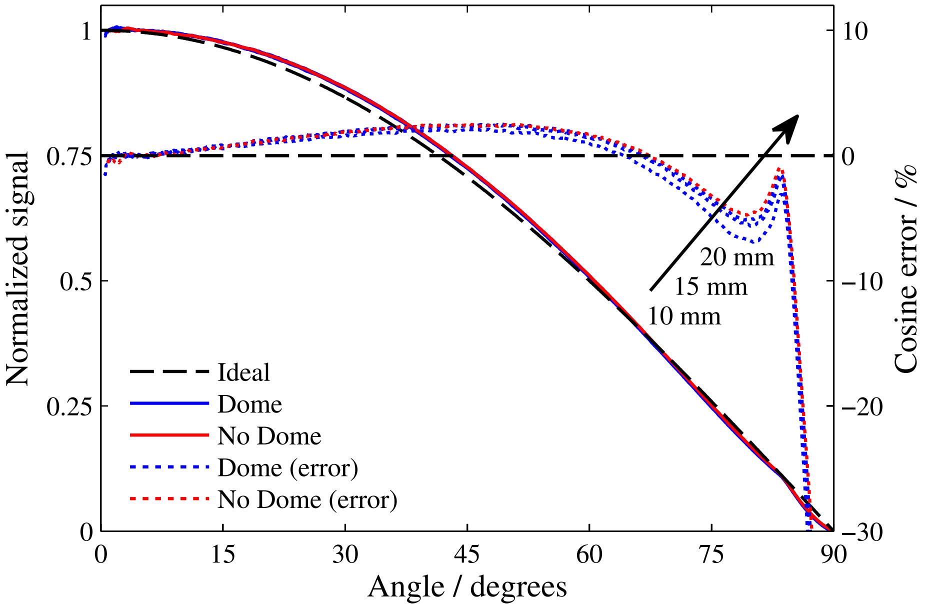

Figure 28: Simulated angular response of a detector at three different weather dome radii (blue lines). The angular response of the detector without a weather dome is shown as a red line. Also plotted is the ideal cosine response (dashed black line).

if one or more of the other simulation parameters are adjusted, the optimal value of the first parameter will be shifted and the optimization process has to be repeated again. This effect is illustrated in Figures 29 where the integrated cosine error f_2 is plotted as a function of the diameter d and the height h of a 2 mm thick diffuser. The difference between the diameter of the diffuser and the diameter of the clear area was kept at $d - d_{\text{beam}} = 2.5$ mm, throughout all the simulations. The shadow ring was aligned with the front surface of the diffuser in each case. For each height – diameter combination, there is an optimal value for the diameter of the shadow ring. However, in the simulations of Figure 29 the value was kept at $d_{\text{sr}} = 35$ mm.

Shaped diffusers introduce a new layer of difficulty to the diffuser optimization process. In Figure 30, the integrated cosine error has been plotted as a function of the radius of curvature of the spherical front surface of the diffuser r_{sph} and the height of the diffuser h. The minimum thickness of the diffuser was $t = 1$ mm and the shadow ring was aligned with the highest part of the diffuser, as illustrated in Figure 16. The diameter of the diffuser and the shadow ring were $d = 11$ mm and $d_{\text{sr}} = 35$ mm, respectively. The difference between the diameter of the diffuser and the diameter of the clear area was $d - d_{\text{beam}} = 2$ mm, in all cases. As can

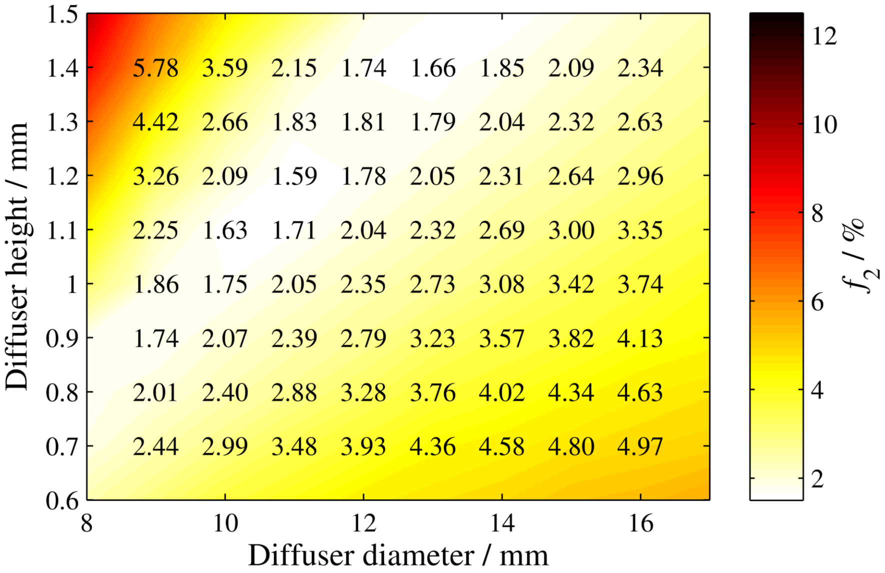

Figure 29: Integrated cosine error plotted as a function of the diameter and the height of the diffuser.

be deduced from Figure 27, changing the clear area of the diffusers would alter the situation dramatically in case of both the flat and the shaped diffusers.

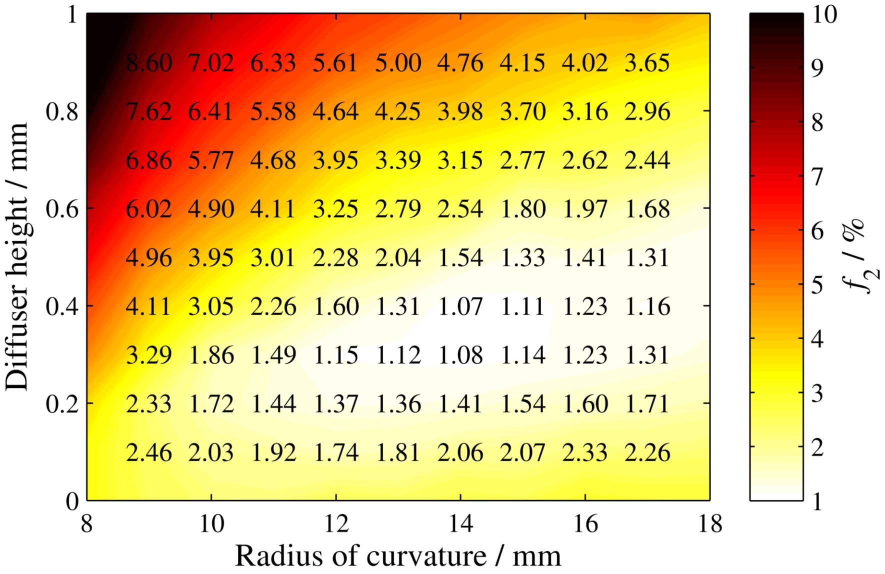

Figure 30: Integrated cosine error plotted as a function of the radius of curvature of the spherical front surface of the diffuser and the height of the diffuser.

The strong linking between the various simulation parameters makes complete, systematic optimization of the diffuser design practically impossible. Furthermore, as each simulation takes at least 10 minutes to complete, common iterative optimization processes, such as Nelder–Mead simplex method [34] used by `fminsearch` function in Matlab, for minimizing f_2 are not practical. For these reasons, some level of trial-and-error is still required to optimize the diffuser.

5.3.2 Optimized diffuser designs

As discussed in Section 2, detector heads with flat diffusers are relatively cheap to produce and are therefore particularly attractive solutions for mass production. On the other hand, better angular responses can be achieved with shaped diffusers. For these reasons, two separate detector structures, one with a raised flat diffuser and the other with a shaped diffuser, were optimized. The light was collected with an optical fiber, at the distance $z_{\mathrm{det}} = 29$ mm from the back surface of the diffuser. The clear area of the diffuser was limited mechanically and not through the acceptance angle of the fiber. A protective weather dome was incorporated in both designs.

The angular response of an optimized raised flat diffuser is shown as a green line in Figure 31. The optimal shape was found by tuning the diameter d and the height h of the diffuser, the diameter of the shadow ring d_{sr} as well as the diameter of the clear area of the diffuser d_{beam}. The optimal values for these parameters were $d = 13$ mm, $h = 1.4$ mm, $d_{\mathrm{sr}} = 35$ mm and $d_{\mathrm{beam}} = 10.5$ mm. The thickness of the diffuser was $t = 2$ mm. For comparison, the angular response of a non-raised diffuser that is otherwise identical to the optimized raised diffuser is plotted in the same figure as the blue line. The results confirm that remarkable improvements in cosine response can be obtained simply by tuning the diffuser height: The calculated integrated cosine error was $f_2 = 7.4$ % for the non-raised diffuser, whereas a value of $f_2 = 1.6$ % was obtained with the optimized raised diffuser.

The solid red line of Figure 31 shows the angular response of the optimized shaped diffuser. The diameter of the diffuser was $d = 11$ mm and the radius of curvature of the spherical surface was $r_{\mathrm{sph}} = 14$ mm. The thickness of the edge of the diffuser was $t = 1$ mm, and the diffuser was raised 0.5 mm relative to the surface of the detector structure. The diameters of the shadow ring and the clear area of the diffuser were $d_{\mathrm{sr}} = 23$ mm and $d_{\mathrm{beam}} = 8.5$ mm, respectively. Introduction of a spherical front surface to the calculations had a drastic effect on the quality of the angular response of the device, and the design yielded an integrated cosine error of just $f_2 = 0.63$ %. This simulated value is lower than the integrated cosine errors of current state of the art detector heads, discussed in Section 2.3.

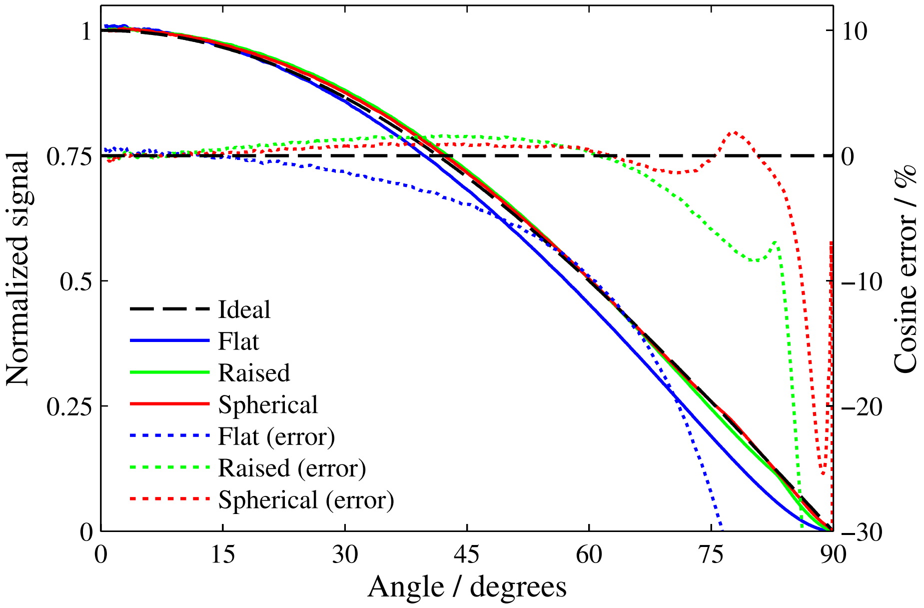

Figure 31: Simulated angular response of a flat diffuser (blue line), an optimized raised flat diffuser (green line), and an optimized shaped diffuser (red line). Also plotted is the ideal cosine response (dashed black line).

6 Conclusions

Two improved detector heads, one with raised flat diffuser and the other with spherically shaped diffuser, for global spectral irradiance measurements were designed. Careful material characterization and thorough optimization of the shape of the diffuser are required to achieve low values of the integrated cosine error. Therefore, a combination of measurements and simulations was used to determine the best material and the optimal shape of the diffuser.

Various material samples were characterized in a goniometric measurement setup where an expanded HeCd laser beam acted as the light source. Novel bubbled quartz materials were found to be attractive alternatives to the more traditional PTFE (Teflon) materials. In general, the quartz materials exhibited lower integrated cosine errors and transmitted significantly more light than PTFE materials of similar thickness. Selected material samples were also studied in a fluorescence spectrometer. Possible fluorescence was at least five orders of magnitude below the intensity of the diffusely reflected component of the excitation wavelength.

The material sample with the lowest integrated cosine error was selected for further study. This quartz sample also had very impressive transmission properties, which means that thicker diffusers can be used without sacrificing the signal-to-noise of the instrument. It remains to be studied how a different material selection criterion would have affected the subsequent shape optimization process.

Monte Carlo particle tracing software was constructed for the purpose of optimizing the structure of the detector head. The software accounted for the shape of the diffuser as well as any surrounding structures – such as the detector sidewalls, the shadow ring and the protective weather dome – that affect the overall shape of the angular response of the detector. A comparison between the angular responses measured with a prototype detector and the simulated results confirmed that the software could adequately describe the light transport in the detector structure. Hence, the software can be used to guide the diffuser optimization process.

The effects of the different diffuser parameters on the overall shape of the angular response were studied extensively. The refractive index difference between the diffuser material and its surroundings causes the angular response of a flat non-raised diffuser to deviate considerably from the ideal cosine response at large angles. This issue is inherent in all volume diffusers, and cannot be remedied by better material selection. Therefore, some form of diffuser shaping is always required to reach near-ideal angular response.

Raising the diffuser enables incoming radiation to pass through the sidewalls of the diffuser, increasing the angular response especially at large angles. This effect is related to the sidewall-to-facet area ratio of the diffuser and its strength can be magnified by decreasing the diameter of the diffuser. Similarly, the larger the area of the diffuser that is visible to the detector, the more the light transmission through the sidewalls of the diffuser will contribute to the signal level. The angular response was found to be extremely sensitive to the variations of the diameter of the clear area of the diffuser near the edges of the diffuser. This finding has several implications on diffuser design.

The distance between the shadow ring and the sidewall of the diffuser determines the angle above which the shadow ring gradually starts blocking more and more of the incoming radiation. While the shadow ring is typically aligned with the front surface of the diffuser to prevent any light from reaching the diffuser at incident angles higher than 90°, it was discovered that the angular response at large incident angles can be improved by slightly lowering the shadow ring with respect to the surface of the diffuser. The protective weather dome was found to have little effect on the overall angular response of the detector, provided that the diameter of the weather dome is large enough as compared to the diameter of the diffuser.

Two diffuser designs – a raised flat diffuser and a spherically shaped diffuser – were optimized. The optimized integrated cosine error of the raised flat diffuser was 1.6 %. For comparison, the integrated cosine error of the same detector head with non-raised diffuser was 7.4 %. More control over the shape of the angular response of the detector can be gained by shaping the front surface of the diffuser. An optimized diffuser with a spherical front surface yielded an integrated cosine error of just 0.63 %.

While good agreement between the measured and simulated results was observed, simulations alone may not be adequate for the complete optimization of the diffuser structure, and some fine-tuning of the parameters may also be required during the manufacturing. The reason for this is the high sensitivity of the angular response to variations in the parameter values in combination with the typical manufacturing tolerances of the mechanics and the possible process variations in material production. Nevertheless, the diffuser simulation software offers a faster and more systematic approach to the diffuser design process than the trial-and-error method of building several prototype diffusers and measuring their angular responses individually. The software also sheds new light on how the diffusers actually work and how various parameters affect the performance of the detector.

References

[1] R. Lucas, T. McMichael, W. Smith and B. Armstrong, ”Solar Ultraviolet Radiation: Global Burden of Disease from Solar Ultraviolet Radiation,” in *Environmental Burden of Disease Series* **No. 13**. Ed. Annette Prüss-Üstün et al. (World Health Organization, Geneva, Switzerland, 2006) 258 p.

[2] G. Seckmeyer et al., ”Part 1: Spectral Instruments,” in *Instruments to Measure Solar Ultraviolet Radiation,* WMO-GAW **No. 125**. (World Meteorological Organization, Geneva, Switzerland, 1999) 31 p.

[3] G. Seckmeyer et al., ”Part 2: Broadband Instruments Measuring Erythemally Weighted Solar Irradiance,” in *Instruments to Measure Solar Ultraviolet Radiation,* WMO-GAW **No. 164**. (World Meteorological Organization, Geneva, Switzerland, 2007) 54 p.

[4] V. Fioletov, L. McArthur, T. Mathews and L. Marrett, ”On the Relationship Between Erythemal and Vitamin D Action Spectrum Weighted Ultraviolet Radiation,” *J. Photochem. Photobiol. B: Biol.* **95**, 9–16 (2009).

[5] R. Setlow and E. Grist, ”Wavelengths Effective in Induction of Malignant Melanoma,” *Proc. Natl. Acad. Sci. USA* **90**, 6666–6670 (1993).

[6] A. Parisi, A. Green and M. Kimlin, ”Diffuse Solar UV Radiation and Implications for Preventing Human Eye Damage,” *Photochem. Photobiol.* **73**, 135–139 (2001).

[7] U. Feister, R. Grewe and K. Gericke, ”A Method for Correction of Cosine Errors in Measurements of spectral UV Irradiance,” *Solar Energy* **60**, 313–332 (1997).

[8] J. Gröbner, M. Blumthaler and W. Ambach, ”Experimental Investigation of Spectral Global Irradiance Measurement Errors Due to a Non Ideal Cosine Response,” *Geophys. Res. Lett.* **23**, 2493–2496 (1996).

[9] B. Barton et al., ”Characterization of New Optical Diffusers Used in High Irradiance UV Radiometers,” Poster presented at NEWRAD 2011, Maui, Hawaii, September 19–23 (2011).

[10] CIE 53 - 1982, *Methods of Characterizing the Performance of Radiometers and Photometers,* (International Commission on Illumination, Vienna, Austria, 1982) 27 p.

[11] J. Gröbner, ”Improved Entrance Optics for Global Irradiance Measurements with a Brewer Spectrophotometer,” *Appl. Opt.* **42**, 3516–3521 (2003).

[12] Bentham, *D6/D7 Cosine Response Diffusers*, device datasheet. `http://www.bentham.co.uk/library.htm`

[13] L. Ylianttila and J. Schreder, ”Temperature Effects of PTFE Diffusers,” *Opt. Mater.* **27**, 1811–1814 (2005).

[14] M. Newman and G. Barkema, *Monte Carlo Methods in Statistical Physics,* 1th Edition (Oxford University Press, United Kingdom, 1999) 496 p.

[15] C. Robert and G. Casella, *Monte Carlo Statistical Methods,* 2nd Edition (Springer, New York, 2004) 676 p.

[16] K. Binder, ”Monte-Carlo Methods,” in *Mathematical Tools for Physicists.* Ed. G. Trigg. 1th Edition (Wiley-VCH, Germany, 2005) 249–280.

[17] N. Metropolis and S. Ulam, ”The Monte Carlo Method,” *J. Am. Statist. Assoc.* **44**, 335–341 (1949).

[18] N. Metropolis, ”The Beginning of the Monte Carlo Method,” *Los Alamos Science*, Special Issue 1987, 125–130 (1987).

[19] R. Eckhardt, ”Stan Ulam, John von Neumann, and the Monte Carlo Method,” *Los Alamos Science*, Special Issue 1987, 131–137 (1987).

[20] D. Hartree, ”The ENIAC, an Electronic Computing Machine,” *Nature* **158**, 500–506 (1946).

[21] S. McCartney, *The Triumphs and Tragedies of the World’s First Computer,* 1th Edition (Walker & Company, New York, 1999) 240 p.

[22] S. van der Walt, S. Colbert and G. Varoquaux, ”The NumPy Array: A Structure for Efficient Numerical Computation,” *Comput. Sci. Eng.* **13**, 22–30 (2011).

[23] J. Hunter, ”Matplotlib: A 2D Graphics Environment,” *Comput. Sci. Eng.* **9**, 90–95 (2007).

[24] S. Behnel, R. Bradshaw and D. Seljebotn, ”Cython Tutorial,” *Proceedings of the 8th Python in Science conference – Proc. SciPy 2009*, Pasadena, California, USA, 4–15 (2009).

[25] M. Matsumoto, ”Mersenne Twister: A 623-Dimensionally Equidistributed Uniform Pseudo-Random Number Generator,” *ACM T. Model. Comput. S.* **8**, 3–30 (1998).

[26] M. Saito, *An Application of Finite Field: Design and Implementation of 128-bit Instruction-Based Fast Pseudorandom Number Generator,* Master’s thesis (Graduate School of Science, Hiroshima University, Japan, 2007) 20 p.

[27] L. Henyey and J. Greenstein, ”Diffuse Radiation in the Galaxy,” *Astrophys. J.* **93**, 70–83 (1941).

[28] L. Wang, S. Jacques and L. Zheng, ”MCML – Monte Carlo Modeling of Light Transport in Multi-Layered Tissues,” *Comput. Meth. Programs. Biomed.* **47**, 131–146 (1995).

[29] L. Wang and S. Jacques, *Monte Carlo Modeling of Light Transport in Multi-layered Tissues in Standard C,* 1th Edition (University of Texas M. D. Anderson Cancer Center, Houston, 1992) 183 p.

[30] A. Witt, ”Multiple Scattering in Reflecting Nebulae. I – A Monte Carlo Approach,” *Astrophys. J. Supplement Series* **35**, 1–6 (1977).

[31] D. Malacara and B. Thompson, *Handbook of Optical Engineering,* 1th Edition (Marcel Dekker Inc., New York, 2001) 978 p.

[32] M. Born and E. Wolf, *Principles of Optics: Electromagnetic Theory of Propagation, Interference and Diffraction of Light,* 7th edition (Cambridge University Press, United Kingdom, 1999) 986 p.

[33] S. Holopainen, F. Manoocheri and E. Ikonen, ”Non-Lambertian behaviour of fluorescence emission from solid amorphous material,” *Metrologia* **46**, 197–201 (2009).

[34] J. Lagarias, J. Reeds, M. Wright and P. Wright, ”Convergence Properties of the Nelder-Mead Simplex Method in Low Dimensions,” *SIAM J. Optim.* **9**, 112–147 (1998).